



























MAMMOTH-Subaru. II. Diverse Populations of Circumgalactic Ly α Nebulae at Cosmic Noon

MINGYU LI ¹ HAIBIN ZHANG ^{1,2} ZHENG CAI ¹ YONGMING LIANG ³ NOBUNARI KASHIKAWA ^{2,4,5} KE MA ¹
XIAOHUI FAN ⁶ J. XAVIER PROCHASKA ^{7,8} BJORN H. C. EMONTS ⁹ XIN WANG ^{10,11,12} YUNJING WU ^{1,6}
SHIWU ZHANG ^{1,13} QIONG LI ¹⁴ SEAN D. JOHNSON ¹⁵ MINGHAO YUE ^{16,6} FABRIZIO ARRIGONI BATTATA ¹⁷
SEBASTIANO CANTALUPO ¹⁸ JOSEPH F. HENNAWI ^{19,20} SATOSHI KIKUTA ⁴ YUANHANG NING ¹
MASAMI OUCHI ^{3,2,21} RHYTHM SHIMAKAWA ²² BEN WANG ^{1,19} WEICHEN WANG ¹⁸ ZHENG ZHENG ²³ AND
ZHEN-YA ZHENG ²⁴

ABSTRACT

Circumgalactic Lyman-alpha (Ly α) nebulae are gaseous halos around galaxies exhibiting luminous extended Ly α emission. This work investigates Ly α nebulae from deep imaging of ~ 12 deg² sky, targeted by the MAMMOTH-Subaru survey. Utilizing the wide-field capability of Hyper Suprime-Cam (HSC), we present one of the largest blind Ly α nebula selections, including QSO nebulae, Ly α blobs, and radio galaxy nebulae down to typical 2σ Ly α surface brightness of $(5 - 10) \times 10^{-18}$ erg s⁻¹ cm⁻² arcsec⁻². The sample contains 117 nebulae with Ly α sizes of 40 - 400 kpc, and the most gigantic one spans about 365 kpc, referred to as the Ivory Nebula. Combining multiwavelength data, we investigate diverse nebula populations and associated galaxies. We find a small fraction of Ly α nebulae have QSOs ($\sim 7\%$), luminous infrared galaxies ($\sim 1\%$), and radio galaxies ($\sim 2\%$). Remarkably, among the 28 enormous Ly α nebulae (ELANe) exceeding 100 kpc, about 80% are associated with UV-faint galaxies ($M_{UV} > -22$), categorized as Type II ELANe. We underscore that Type II ELANe constitute the majority but remain largely hidden in current galaxy and QSO surveys. Dusty starburst and obscured AGN activity are proposed to explain the nature of Type II ELANe. The SED of stacking all Ly α nebulae also reveals signs of massive dusty star-forming galaxies with obscured AGNs. We propose a model to explain the dusty nature where the diverse populations of Ly α nebulae capture massive galaxies at different evolutionary stages undergoing violent assembling. Ly α nebulae provide critical insights into the formation and evolution of today's massive cluster galaxies at cosmic noon.

Keywords: galaxies: high-redshift – circumgalactic medium - intergalactic medium: emission lines

1. INTRODUCTION

Hydrogen Lyman-alpha (Ly α) nebulae are gaseous halos of extended Ly α emission around galaxies, tracing enormous reservoirs of hydrogen gas out to the circumgalactic medium (CGM, Tumlinson et al. 2017; Faucher-Giguère & Oh 2023) and intergalactic medium (IGM) scales. Ly α nebulae were first detected as giant halos around high-redshift radio galaxies (HzRGs; McCarthy et al. 1987) and quasi-stellar objects (QSOs;

Hu & Cowie 1987; Heckman et al. 1991). The subsequent discovery referred to as Ly α blobs (Steidel et al. 2000), lacking bright ultraviolet (UV) continuum or radio sources, represented a distinct category. The mysterious power mechanisms of blobs have attracted significant observational and theoretical work aimed at identifying larger samples (*e.g.*, Matsuda et al. 2004; Palunas et al. 2004; Saito et al. 2006; Yang et al. 2009) and explaining the origin of their luminous Ly α emission (*e.g.*, Villar-Martin et al. 1997; Taniguchi & Shioya 2000; Cantalupo et al. 2005; Fardal et al. 2001). The study of Ly α nebulae has since expanded to encompass diverse populations.

With the development of modern observing facilities and instruments, Ly α nebulae have been discovered across cosmic time with diverse observed properties

Corresponding author:
zcaic@mail.tsinghua.edu.cn

lmytime@hotmail.com

hbz@icrr.u-tokyo.ac.jp

(Schirmer et al. 2016; Barger et al. 2012; Zhang et al. 2020; Farina et al. 2019). In general, Ly α nebulae are a rare population of sources, having high Ly α luminosities ($L_{\text{Ly}\alpha} \gtrsim 10^{43}$ erg s $^{-1}$) and large spatially extended Ly α emitting regions ($\gtrsim 40$ kpc). An extreme subclass called enormous Ly α nebulae (ELANe) has been revealed at cosmic noon ($z \simeq 2 - 3$) in past decades (*e.g.*, van Ojik et al. 1997; Reuland et al. 2003; Villar-Martín et al. 2003; Miley et al. 2006; Cantalupo et al. 2014; Hennawi et al. 2015; Cai et al. 2017a; Arrigoni Battaia et al. 2018a). ELANe represent the extremes of Ly α nebulosities with higher Ly α luminosity ($L_{\text{Ly}\alpha} \gtrsim 10^{44}$ erg s $^{-1}$) and larger extent ($\gtrsim 100$ kpc). The detection of such enormous Ly α nebulae provides unique insights into massive CGM gas flows and accretion at the peak epoch of galaxy growth.

A few studies use Ly α nebulae to examine the galactic “ecosystem” comprising IGM, CGM, embedded galaxies, and supermassive black holes (SMBHs). They provide direct observational access to the densest part of the IGM and CGM, enabling studies of gas accretion, feedback, and recycling (*e.g.*, Arrigoni Battaia et al. 2018a; Ao et al. 2020; Wang et al. 2021; Li et al. 2021; Daddi et al. 2021; Zhang et al. 2023b, 2024). In contrast to these Ly α nebulae, however, in most other systems, the CGM/IGM is usually too faint to be visible in emission and can only be detected through absorption along just a few sightlines (*e.g.*, Zhu & Ménard 2013; Napolitano et al. 2023; Zou et al. 2024; Wu et al. 2023). Ly α nebulae, therefore, represent rare and unique opportunities to survey the formation and evolution of the galaxy in the early universe (Ouchi et al. 2020).

Several observational techniques have been utilized to identify Ly α nebulae. Narrowband imaging surveys are the first and remain one of the most effective approaches (*e.g.*, Fynbo et al. 1999; Keel et al. 1999; Francis et al. 2001; Palunas et al. 2004; Dey et al. 2005; Nilsson et al. 2006; Smith & Jarvis 2007; Ouchi et al. 2008; Matsuda et al. 2009; Yang et al. 2010; Erb et al. 2011; Matsuda et al. 2011; Cantalupo et al. 2012; Kikuta et al. 2017; Shibuya et al. 2018; Kikuta et al. 2019; Rahna et al. 2022; Ramakrishnan et al. 2023). Similarly, medium-band and broad-band imaging have also proved useful for finding luminous Ly α nebulae based on color excess (*e.g.*, Saito et al. 2006; Prescott et al. 2012; Barger et al. 2012; Hibon et al. 2020; Shimakawa 2022). More recently, integral field spectrograph/unit (IFS/IFU) instruments on 8-10m class telescopes, such as VLT/MUSE and Keck/KCWI, have enabled the most comprehensive studies of Ly α nebulae both for blind but small field-of-view surveys (*e.g.*, Caminha et al. 2016; Vanzella et al. 2016; Leclercq et al. 2017; Kusak-

abe et al. 2022) and targeted follow-up of pre-selected sources (*e.g.*, Borisova et al. 2016; Arrigoni Battaia et al. 2019; Cai et al. 2019).

Nevertheless, most of the discovered nebula samples still rely on pre-selections of individual targets, which may lead to an incomplete picture of the whole Ly α nebulae population. Ly α nebulae are thought to relate to the formation of massive galaxies whose dark matter halo has a typical mass of $\sim 10^{13}M_{\odot}$, living in the most active star formation region and trace large-scale mass overdensities. Therefore, one successful pre-selection technique is to target biased tracers of massive halos, such as luminous QSOs (*e.g.*, Borisova et al. 2016; Arrigoni Battaia et al. 2016, 2019; Cai et al. 2019; Farina et al. 2019; Mackenzie et al. 2021), high-redshift radio galaxies (*e.g.*, Swinbank et al. 2015; Wang et al. 2021), active galactic nucleus (AGN) pairs/groups (*e.g.*, Hennawi et al. 2015; Cai et al. 2018), galaxy groups/clusters (*e.g.*, Daddi et al. 2021, 2022; Jiménez-Andrade et al. 2023), and dust-obscured galaxies (*e.g.*, Bridge et al. 2013; Ginolfi et al. 2022).

A wide-field survey independent of individual target pre-selections is needed to study the diverse population of Ly α nebulae comprehensively. Compared to blind fields, Ly α nebulae, especially ELANe, tend to reside in high-redshift overdense regions (*e.g.*, Steidel et al. 2000; Dey et al. 2005; Matsuda et al. 2005; Prescott et al. 2009; Yang et al. 2010; Hennawi et al. 2015; Cai et al. 2017a,b, 2018; Arrigoni Battaia et al. 2018a). Therefore, the effects of nebula clustering in overdensity will enable the discovery of more and larger Ly α nebulae.

Based on the selection with QSO spectra as sightlines (*e.g.*, Cai et al. 2017a), we construct a sample of large-scale structures at $z = 2 - 3$, using IGM Ly α forest absorption, *i.e.*, coherently strong Ly α absorption system (CoSLA) as tracers (Cai et al. 2016). Pilot surveys successfully identify a few massive protoclusters at $z = 2 - 3$, *e.g.*, BOSS1441 (Cai et al. 2017b), BOSS1244, and BOSS1542 (Zheng et al. 2020; Shi et al. 2021). An ELAN dubbed MAMMOTH-1 (Cai et al. 2017a) was discovered close to the density peak of protocluster BOSS1441, which has a spatial extent of over 400 kpc and the highest extended Ly α luminosity to date. Such an extreme ELAN provides a great opportunity to systematically study CGM gas flows directly to reveal aspects of galaxy evolution.

Encouraged by the successful pilot study, we have constructed a larger sample of eight MAMMOTH fields using Subaru Hyper Suprime-Cam (Subaru/HSC; Miyazaki et al. 2018), and this project is named MAMMOTH-Subaru (also see Liang et al. 2021; Zhang et al. 2023a, 2024; Ma et al. 2024; Liang et al. 2024,

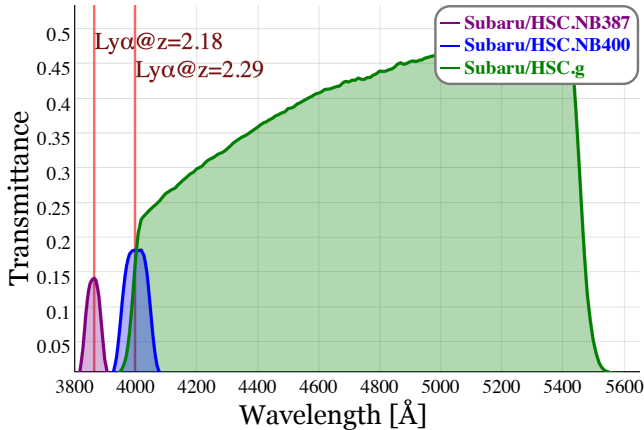


Figure 1. Transmission curves of NB387, NB400, and g band mounted on the HSC. The purple, blue, and green solid lines (from left to right) represent the total transmittance of NB387, NB400, and g band respectively. Two red vertical lines denote the wavelength of the redshifted $\text{Ly}\alpha$ line at $z = 2.18$ and $z = 2.29$. This figure is generated by our interactive web application [MyFilter](#).

Liang et al. in prep.). Thanks to the sufficiently wide field of view (FoV) of HSC (1.5° diameter), the deep narrowband imaging in these fields allows us to construct a complete sample of $\text{Ly}\alpha$ nebulae, without the need for pre-selection of powering sources (e.g., Type-I QSO). Therefore, our sample can represent a comprehensive view of the $\text{Ly}\alpha$ nebula population powered by various sources and mechanisms.

In this paper, we investigate a large sample of $\text{Ly}\alpha$ nebulae at $z \sim 2.2 - 2.3$, selected from a wide, deep narrowband imaging survey. The structure of this paper is as follows: In §2, we describe our observations and data reduction procedures. In §3, we present the sample selection for $\text{Ly}\alpha$ nebulae. In §4, we report the nebula sample, show the results of observed diversity in multi-wavelength properties, and propose a picture to explain the diverse population. In §6, we summarize this work and present brief conclusions. In this work, we use the vacuum wavelength 1215.670\AA for $\text{Ly}\alpha$ based on the Atomic Line List v2.04¹. Throughout this paper, magnitudes are given in the AB system (e.g., Oke 1974; Oke & Gunn 1983) unless otherwise specified. We adopt a flat Λ CDM cosmology with $\Omega_{m,0} = 0.3$ and $H_0 = 70 \text{ km s}^{-1} \text{ Mpc}^{-1}$. In this cosmology, at the redshift $z = 2.18$, $1''$ corresponds to a physical 8.28 kpc ; at the redshift $z = 2.29$, $1''$ corresponds to $8.21 \text{ physical kpc}$.

¹ <https://linelist.pa.uky.edu/atomic/index.html>

2. OBSERVATIONS AND DATA

Our survey covers eight SDSS/(e)BOSS fields (see Table 1) selected based on the MAMMOTH approach and/or QSO clustering (Cai et al. 2016; Liang et al. 2021, 2024, Liang et al. in prep.). The Subaru observations took deep narrowband and broadband imaging for these eight fields. Furthermore, we performed spectroscopic observations for a few selected $\text{Ly}\alpha$ nebulae. The observation details are as follows.

2.1. Imaging Observations

In this section, we summarize the Subaru imaging observations in programs S17B-041 (PI: N. Kashikawa), S19A-TE288, S19B-ChinaTAP (PI: Z. Cai), and S20A-108 (PI: Y. Liang), but please see Liang et al. (2021) and Liang et al. (in prep.) for details.

In our survey, we perform deep narrowband imaging using NB387 ($\lambda_c=3863\text{\AA}$, $\Delta\lambda=55\text{\AA}$) and NB400 ($\lambda_c=4003\text{\AA}$, $\Delta\lambda=92\text{\AA}$) filters on the HSC, which covers 1.5° FoV in diameter. The narrowband filters enable us to detect $\text{Ly}\alpha$ emission at the corresponding redshifts of $z = 2.177 \pm 0.023$ and $z = 2.293 \pm 0.038$, respectively. The line-of-sight depth of the redshift slice is 62.3 cMpc for NB387 and 97.8 cMpc for NB400. The HSC-g band ($\lambda_c=4754\text{\AA}$, $\Delta\lambda=1395\text{\AA}$) is used for the continuum estimate of the line-emitting sources. The transmission curves of these three filters are shown in Figure 1, which is generated by our interactive web application [MyFilter](#)²(Li 2023).

The HSC imaging data were reduced using the HSC pipeline, [hscPipe](#) (Bosch et al. 2018). The details of imaging reductions can be checked in Liang et al. (2021). Here we present a brief summary of the reduction procedures. First, the primary calibration data (i.e., the bias, dark, flat, and global sky) were made. Then they were applied to each visit. Pan-STARRS DR1 (Flewelling et al. 2020) catalogs are regarded as references for astrometry and photometry. Finally, the coadding process was performed for each visit to generate mosaic image products. Note that systematic photometry corrections due to the stellar metallicity bias were included in our reduction, which addresses a known issue also reported in the HSC Subaru Strategic Program (SSP; Aihara et al. 2019, 2022).

2.2. Spectroscopic Observations

² <https://github.com/lmytime/MyFilter>

Table 1. Summary of field information

Field	R.A.	Decl.	Obs Period	θ_{NB}	θ_{BB}	$m_{\text{NB},5\sigma}$	$m_{\text{BB},5\sigma}$	Area	Ly α SB $_{2\sigma}$
name	hh:mm:ss.ss	dd:mm:ss.s	month, year	arcsec	arcsec	mag	mag	deg 2	10^{-18} cgs. arcsec $^{-2}$
(1)	(2)	(3)	(4)	(5)	(6)	(7)	(8)	(9)	(10)
J0210	02:09:58.90	+00:53:43.0	Jan., 2018	1.22	0.90	24.25	26.34	1.34	10.56
J0222	02:22:24.66	-02:23:41.2	Jan., 2018	0.90	0.90	24.99	27.01	1.13	8.23
J0924	09:24:00.70	+15:04:16.7	Jan. & Mar., 2019	0.84	0.79	24.74	26.63	1.47	9.79
J1419	14:19:33.80	+05:00:17.2	Mar., 2019	0.86	0.70	24.81	26.80	1.45	10.66
J0240	02:40:05.11	-05:21:06.7	Nov., 2019	1.00	0.84	25.61	26.80	1.53	7.78
J0755	07:55:35.89	+31:09:56.9	Nov., 2019	0.88	1.16	25.83	26.50	1.54	5.04
J1133	11:33:02.40	+10:05:06.0	Mar., 2020	0.85	0.82	25.49	26.30	1.55	9.19
J1349	13:49:40.80	+24:28:48.0	Mar., 2020	0.98	0.86	25.67	26.15	1.62	7.76

NOTE—(1) the name of fields; (2-3) field center coordinates Right Ascension and Declination in equinox with an epoch of J2000; (4) the period of executing the observations; (5-6) the FWHMs of PSFs measured by PSFEx; (7-8) are the 5σ limiting magnitudes measured in an aperture with the radius of $1.7''$ ($2.5''$ for J0210 field to match the seeing) for the final stacked NB and g -band image, respectively; (9) the effective survey area after masking; (10) the average 2σ detection limit of Ly α line map in unit of 10^{-18} erg s $^{-1}$ cm $^{-2}$ arcsec $^{-2}$.

We take follow-up spectroscopic observations for a few selected Ly α nebula candidates (see section §3 for the selection) using the MMT/Binospec spectrograph (Fabricant et al. 2019) and the Magellan/IMACS spectrograph (Dressler et al. 2011).

The observations of MMT/Binospec are carried out in April 2021 and July 2022. We use the long-slit mode of Binospec with $1''$ width and $2'$ length to take the spectra. Different instrument configurations are used for April and July observations. In the April observations, we adopt the LP3500 filter and the 1000 lines/mm grating (1000 lpm mode hereafter), which allows photons from 3720 \AA to 4950 \AA with the spectral resolution of $R \simeq 3900$. Each source is taken for $10 \times 1200 \text{ s} = 3.3 \text{ hrs}$. In the July observations, we use the LP3800 filter and 600 lines/mm grating (600 lpm mode hereafter), covering from 4000 \AA to 6400 \AA with $R \simeq 2740$. The integration time is $4 \times 1200 \text{ s} = 1.3 \text{ hrs}$. The Binospec setting allows coverage of the redshifted emission lines, including Ly α and N V for sources at $z \simeq 2$. We reduce the Binospec data using the official IDL pipeline (Kansky et al. 2019).

The observations of Magellan/IMACS are taken on September 29 and 30, 2022, using the multi-slit spectroscopy mode with the f/2 camera. The field of view of IMACS is a circle with a radius of $12''$. We use the 400 lines per mm grism combined with a custom filter to cover the wavelength between $\simeq 3600 \text{ \AA}$ and 5700 \AA . The spectral resolution is $\sim 7 \text{ \AA}$ using this setup with a slit width of 1.2 arcsec and slit length of

8.0 arcsec . We observe one pointing in each of the J0210 and J0222 fields for NB387 sources, and two pointings in the J0240 field for NB400 sources. The on-source exposure times are 7500 s for NB387 fields and 6000 s for NB400 fields. We reduce the spectroscopic data using the official pipeline COSMOS (Oemler et al. 2017).

3. SAMPLE SELECTION

The Ly α nebula samples are selected through three steps: (1) constructing source detection and photometry catalog; (2) selecting emitters based on color excess of the narrow-band (NB) compared to the broad-band (BB); (3) identifying nebulae based on their extended area. While similar to the Ly α emitter (LAE) selection with the same HSC images (Liang et al. 2021; Zhang et al. 2024), the procedure for searching for Ly α nebulae requires some optimal adjustments of source detection, which are detailed in this section.

3.1. Photometry Catalog and Emitter Selection

We construct photometric catalogs in the narrow-band (NB387 or NB400) and broad-band (g -band) mainly using SExtractor 2.25.0 (Bertin & Arnouts 1996). Firstly, we use Astropy to crop and correct the NB and BB images to the same shape and refine them to the same world coordinate system (WCS). We run SExtractor in dual-image mode with the narrow-band images as detection references. The detection threshold is set as 15 continuous pixels over the 2σ sky background. To match the seeing, we adopt a 7×7 convolution mask of a Gaussian kernel with FWHM = 3.0

pixels to smooth the image before source detection. We apply the sky background root-mean-square (RMS) map as the weighting map to minimize the slight image depth fluctuation effect. Besides, we set the global background mode with a mesh size of 128 pixels. Finally, the narrowband and broad-band source catalogs are combined naturally. We manually make masks to remove the sources in the regions around saturated stars, with severe artifact contamination and with severe stray lights. Please check Table 1 for the field survey areas of our eight fields after masking. When the objects in the broadband are fainter than the 2σ limiting magnitude (see Table 1), we replace their magnitude with the corresponding 2σ limiting magnitude for color excess analysis.

We simultaneously adopt Kron-like elliptical aperture magnitudes (MAG_AUTO) and circular aperture magnitudes (MAG_APER) to derive photometric properties. The aperture radii are set to be 10 pixels $\simeq 1.7''$ (15 pixels $\simeq 2.5''$ for the J0210 field due to the poor seeing) to match the seeing. The point spread function (PSF) is measured when constructing the photometry catalog using PSFEx 3.17.1 (Bertin 2011). The FWHM value of the PSF is used for the PSF-matching procedure between the narrowband and broadband images.

Based on the detection and photometry catalog constructed using the methods shown above, we apply the same selection criteria as shown in Liang et al. 2021; Zhang et al. 2024 to select emitters with a rest-frame Ly α equivalent width $EW_0 > 20\text{\AA}$. It should be noted that the criteria may select a few unmasked stray lights, hot pixels, moving objects, saturated objects, and other artifacts. Visual inspection is conducted to eliminate them. For see further details on emitter selection, please refer to Ma et al. (2024) and Zhang et al. (2024).

3.2. Emission Line Map and Nebula Selection

We make line emission images (Ly α images) to measure the luminosity and spatial extent of Ly α emission to select nebulae. Before making the Ly α image, we match the PSF between the NB and BB image using a Gaussian kernel with FWHM of measured PSF (see Table 1). We use a linear combination of the NB and BB images with different coefficients to produce the continuum and Ly α image. For NB387 emitters, the equations are:

$$f_{\nu,\text{cont}} = \langle f_{\nu} \rangle_{\text{g}},$$

$$F_{\text{Ly}\alpha} = (\langle f_{\nu} \rangle_{\text{NB387}} - \langle f_{\nu} \rangle_{\text{g}}) \cdot \frac{c \cdot 55.9 \text{ \AA}}{(3862.0 \text{ \AA})^2}; \quad (1)$$

and for NB400 emitters, the equations are:

$$f_{\nu,\text{cont}} = 1.027 \langle f_{\nu} \rangle_{\text{g}} - 0.027 \langle f_{\nu} \rangle_{\text{NB400}},$$

$$F_{\text{Ly}\alpha} = (\langle f_{\nu} \rangle_{\text{NB400}} - \langle f_{\nu} \rangle_{\text{g}}) \cdot \frac{c \cdot 101.0 \text{ \AA}}{(4000.9 \text{ \AA})^2}. \quad (2)$$

In these equations, $\langle f_{\nu} \rangle_{\text{g}}$, $\langle f_{\nu} \rangle_{\text{NB387}}$, and $\langle f_{\nu} \rangle_{\text{NB400}}$ denote the measured flux density in each filter and c is the light speed in vacuum. Please refer to Appendix A for the detailed definition, methodology, and derivation of these equations.

Note that the above equations are based on two assumptions. One assumption is that the continuum flux density of Ly α emitting sources is $f_{\nu} = \text{constant}$ (or $f_{\lambda} \propto \lambda^{\beta}$ where the slope $\beta = -2$). The other assumption is that we assume the emission line is described by a delta function with the pivot wavelength of the narrowband as the line wavelength. Different assumed UV slopes could affect the Ly α luminosity estimate, but the effects are tested to be within about 0.1 dex (*e.g.*, Liang et al. 2021). If the true line wavelength is offset from the pivot wavelength, we will underestimate the line flux. Therefore, note that the estimated line fluxes are lower limits due to these systematic issues.

We measure the limiting surface brightness for the Ly α images in the eight fields and presented them in Table 1. The typical 2σ limiting surface brightness is $SB_{2\sigma} = 5 - 10 \times 10^{-18} \text{ erg s}^{-1} \text{ cm}^{-2} \text{ arcsec}^{-2}$ measured by the pixel-to-pixel fluctuation. Based on the Ly α image, we run SExtractor in association mode to measure the isophotal area and isophotal flux of selected LAEs over the 2σ limiting surface brightness. We derive the Ly α luminosity from the line flux assuming the Ly α at redshift $z = 2.18$ for NB387 and $z = 2.29$ for NB400. To distinguish between point-like Ly α emitting sources and extended nebulae in our observation depth, we require the isophotal area of candidate nebulae to be larger than that of the point sources. The point-like sources in each field are identified from the half-flux radii $r_{0.5}$ v.s. magnitude diagram. The half-flux radii of point sources are almost constant and only depend on the FWHM of PSF, leading to horizontal sequences in the $r_{0.5}$ v.s. magnitude diagram. We select these point sources within the 1σ confidence level of the sequence.

We use these point-like sources as references to determine whether our selected emitters have extended emission profiles. Assuming that all the flux in the narrowband for the point source comes from Ly α emission, we can mark these point sources on the area v.s. luminosity figure, and they are arranged in a linear sequence (black dots in Figure 2). The areas of nebulae are required to be 3σ above this point source sequence, where σ is the

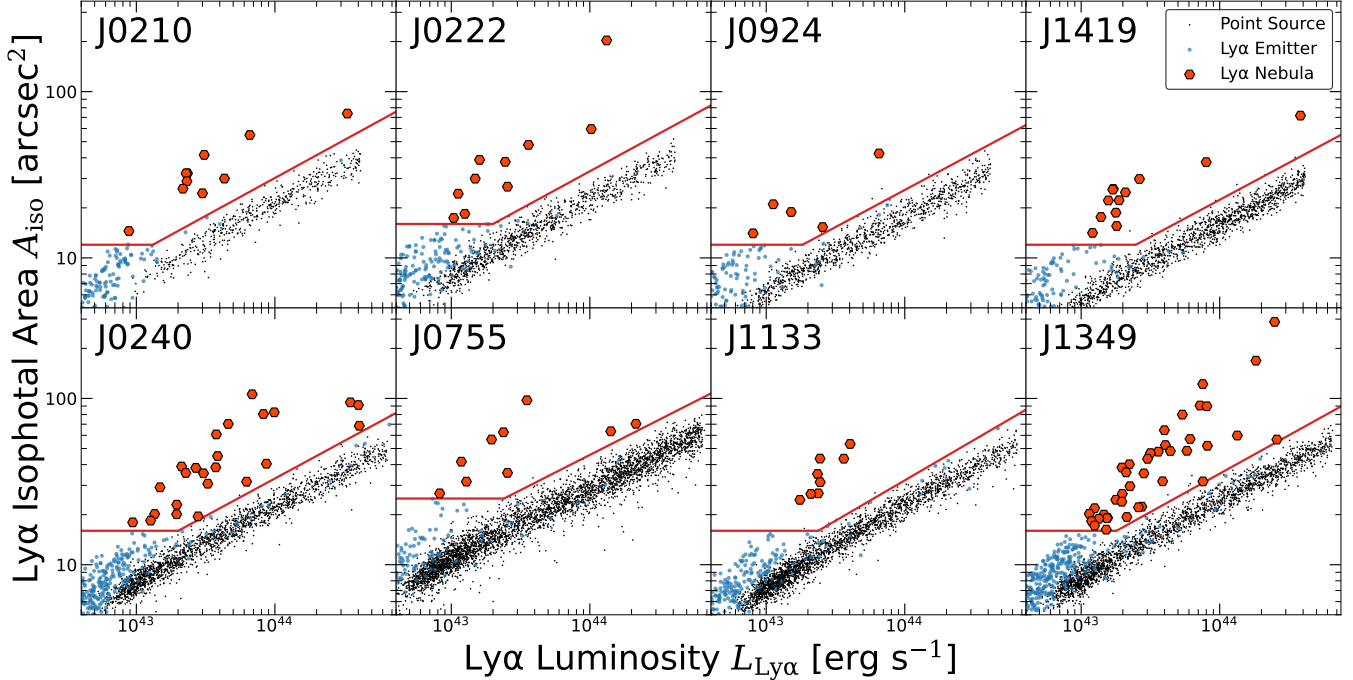


Figure 2. Isophotal areas (A_{iso}) versus $\text{Ly}\alpha$ luminosity ($L_{\text{Ly}\alpha}$) of selected $\text{Ly}\alpha$ nebulae in our eight fields. Blue dots represent $\text{Ly}\alpha$ emitters (LAEs), and red hexagons denote selected nebulae. The inclined lines denote the 3σ above the sequence of point sources (black dots), indicating that the sources above have spatially extended profiles. The nebula selection criteria are bounded to the upper side by the red lines. Our selected nebulae are located well above this relation.

root mean square error of the linear regression for the sequences. Note that it is difficult to distinguish the point source and the extended source if the source has faint diffuse emission. Consequently, we require additional minimal area criteria for a robust nebula selection. The minimal areas are chosen to match the different detection limits of our eight fields. The previous literature (*e.g.*, Kimock et al. 2021; Yang et al. 2009, 2010; Bădescu et al. 2017) gave a few different minimal area criteria despite considering the disparity of depths. We refer to the simulation of Kimock et al. (2021) to give an estimate of $\text{Ly}\alpha$ extended area for nebulae at $z = 2$. The criteria of minimal area are chosen to match the imaging depth as 12 arcsec^2 for J0210, J0924, and J1419 fields; 16 arcsec^2 for J0222, J0240, J1133, and J1349 fields; 25 arcsec^2 for J0755 field. We adopt tests to fine-tune the minimal area criteria from $10 - 30 \text{ arcsec}^2$, which suggested that our final criteria choice minimized the spurious detection and achieved almost the highest completeness. The criteria and procedure of nebula selections are shown in Figure 2.

We visually inspect these nebulae and checked individual exposures to remove any fake selections. Fake selections include stray light, moving objects, artifacts, and objects that have been confirmed at $z < 2$ (*e.g.*, Flesch 2021). Note that we exclude five sources that are contaminated by foreground galaxies or stars, whose

isophotal areas can be unexpectedly boosted. Based on our selection and visual inspection, 117 $\text{Ly}\alpha$ nebulae are selected in eight fields. We index the sample according to the $\text{Ly}\alpha$ isophotal area (from largest to smallest) in the format of “MLANid”, where MLAN represents the abbreviation of MAMMOTH $\text{Ly}\alpha$ nebula. The ids, equatorial coordinates, photometry magnitudes, $\text{Ly}\alpha$ luminosities, isophotal areas, and end-to-end extents of our nebula sample are shown in Table 2.

3.3. Spectroscopic confirmation

We have carried out spectroscopic observations with MMT/Binospec and Magellan/IMACS for seven of our nebula candidates (MLAN1, MLAN3, MLAN10, MLAN52, MLAN64, and MLAN84). The spectra of four nebulae are taken by Binospec with MLAN1, MLAN3, and MLAN52 in 1000 lpm mode and MLAN10 in 600 lpm mode (see Section 2.2). Three nebulae (MLAN14, MLAN84, and MLAN64) are assigned in the slit of the IMACS mask.

Overall, we capture spectra for a total of seven sources. All these sources are confirmed successfully, and some of them have been detected with other emission lines (*e.g.*, N V, C IV, and He II) in addition to $\text{Ly}\alpha$. We use a Gaussian profile to fit the emission lines to determine the redshift based on the best-fit Gaussian centroid. The redshifts of MLAN14, MLAN64, and

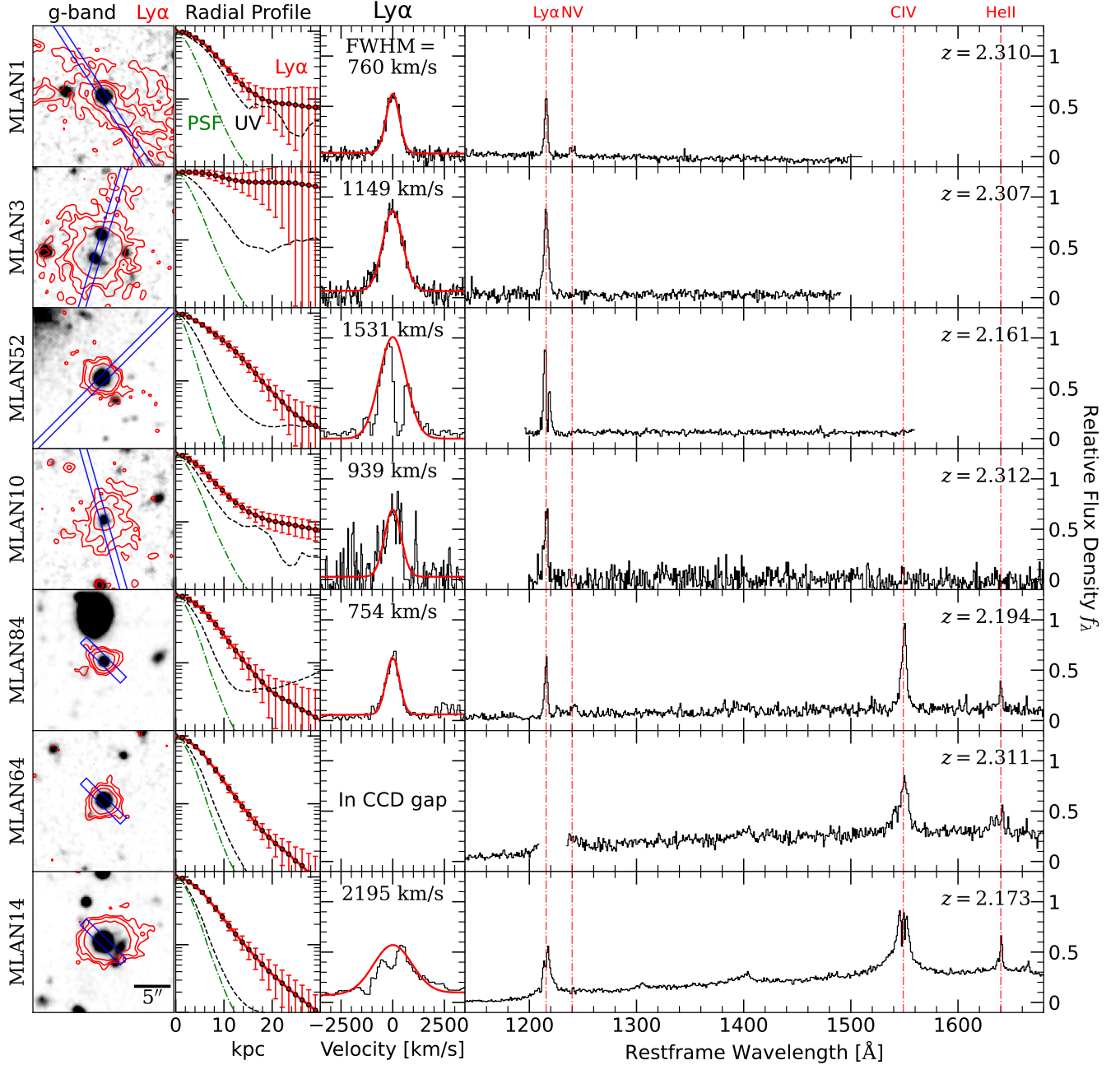


Figure 3. Cutout images, radial profile, and spectra of spectroscopically confirmed $\text{Ly}\alpha$ nebulae. Each row presents one object. For each object, the left panel shows the g-band image with overlaid $3, 5, 10\sigma$ $\text{Ly}\alpha$ contours (red lines). The blue rectangles denote the positions of spectroscopic slits. The middle-left panels show the surface brightness radial profiles of $\text{Ly}\alpha$, UV continua, and PSF with the image center in the left panels as the profile center. The right panels present the extracted 1D spectrum in the rest frame with redshift noted. The middle-right panels zoom into the $\text{Ly}\alpha$ wavelength in relative velocity space and red lines denote the best-fit of the $\text{Ly}\alpha$ emission lines with FWHM annotated at the top.

MLAN84 are based on the He II line, and the redshifts of others are based on the Ly α lines. For MLAN52, we mask the “absorption” in the Ly α line to fit a Gaussian profile. The Ly α lines of our confirmed Ly α nebulae have typical FWHM $\gtrsim 700$ km s $^{-1}$, much larger than the typical LAE Ly α line FWHM $\lesssim 400$ km s $^{-1}$ (e.g., Kerutt et al. 2022; Ning et al. 2020, 2022). The broad line features, large equivalent width, and coexisting lines indicate that the emission line captured by NB is Ly α , and these objects are Ly α nebulae. The extracted spectra and the best-fit redshifts of these seven sources are shown in Figure 3. Meanwhile, we also show the cutout images with overlaid Ly α contours and surface brightness radial profiles in Figure 3.

Note that there may be contamination of other extended line emitters, e.g., [O II] $\lambda 3728$ at $z \simeq 0.035$ for NB387 ($z \simeq 0.07$ for NB400), Mg II $\lambda 2800$ at $z \simeq 0.4$, C III] $\lambda 1908$ at $z \simeq 1$, and C IV $\lambda 1549$ at $z \simeq 1.5$. However, previous works using a similar selection approach show that the contamination rate is minimal ($\lesssim 1\%$) (e.g., Matsuda et al. 2004; Yang et al. 2010; Bădescu et al. 2017) because of small survey volume at low- z and the rarity of high EW emission lines³. In addition, the one hundred percent confirmation rate of our spectroscopic observations indicates that our criteria can guarantee a high purity of the sample.

4. RESULTS

4.1. A large sample of Ly α nebulae

Taking a deep narrowband imaging survey covering an effective area of $\simeq 12$ deg 2 , we reveal 117 Ly α nebulae at redshift $z = 2.1 - 2.3$. This nebula sample significantly increases the number of known extended Ly α nebulae at this epoch. These nebulae have Ly α luminosities ranging from 8×10^{42} erg s $^{-1}$ to 4×10^{44} erg s $^{-1}$ and isophotal areas of 14–290 arcsec 2 . It is noteworthy that out of 117 nebulae, there are 28 nebulae in our sample with an end-to-end Ly α size over 100 kpc, categorized as ELANe.

In Figure 4, we show the Ly α luminosities, isophotal areas, and maximum projected sizes of our sample. For comparison, we overlay results from previous studies (Kikuta et al. 2019; Yang et al. 2010; Arrigoni Battaia et al. 2019; Matsuda et al. 2004, 2011; Borisova et al. 2016; Bădescu et al. 2017; Hennawi et al. 2015; Cantalupo et al. 2014; Cai et al. 2017b). However, direct

comparisons between studies should be made cautiously due to different selection methods, sensitivity, and redshifts between surveys. For example, the isophotal areas and sizes were measured using different narrowband filters and luminosity limits. Therefore, we refrain from over-interpreting the comparisons.

We find that there is a field-to-field variation in nebula number densities for our eight fields, as no significant difference exists between survey depth and survey area. This variation can indicate strong clustering of the nebulae, as analyzed by Zhang et al. (2023a) and in our future work.

4.2. Ivory Nebula: Discovery of an intergalactic nebula

We report the discovery of MLAN1, the largest nebula in our sample. To emphasize its exceptional properties, we have given this nebula the nickname “Ivory Nebula”. The Ly α line map for Ivory Nebula shows extended filamentary structure and well-resolved clumpy Ly α emission along the direction of two galaxies (see Figure 5). Ivory Nebula has a Ly α luminosity of $L_{\text{Ly}\alpha} = 2.5 \times 10^{44}$ erg s $^{-1}$ and an end-to-end angular extent of $D \simeq 44.4'' \simeq 365$ kpc. The extreme properties make it one of the largest and most luminous intergalactic nebula discovered in the Universe.

We obtained a long-slit spectrum for the Ivory Nebula along the axis connecting its two associated galaxies (indicated by the yellow lines in the right panel of Figure 5). The spectra, zoomed in on the wavelength region surrounding the Ly α emission line, are shown in Figure 5. We detect and confirm the presence of spatially extended Ly α emission from this spectacular nebula. Strikingly, the 2D spectra reveal complex kinematics of the Ly α emitting gas. Based on the peaks in the Ly α line flux map, we divide the nebula into three components (A, B, and C, as indicated in Figure 5) along the slit.

Component A is a galaxy with a g-band magnitude of $m_g = 24.08$. In addition to Ly α , the spectra show N V $\lambda\lambda 1238.8, 1242.8$ doublet emission. To make the highly ionized N V emission line possible, N $^{4+}$ with $h\nu > 77.5$ eV is required, indicating the presence of an AGN in the component A. The Ly α line profile of A consists of a broad component with FWHM = 831 km s $^{-1}$ and a narrow Ly α spike with FWHM = 130 km s $^{-1}$, shown in Figure 5. Component B can be a diffuse Ly α -emitting gaseous “dark cloud” (e.g., Cantalupo et al. 2012) without a UV continuum counterpart. Component C is another faint continuum source with a g-band magnitude of $m_g = 24.36 \pm 0.06$, which is surrounded by a luminous Ly α -emitting cloud with a complicated double-peak feature. It is noteworthy that Ly α emission peak offsets from the component C about $2.5''$.

³ For example, [O II] $\lambda 3728$ emitters at low- z rarely have rest-frame equivalent width larger than 100Å (e.g., Hogg et al. 1998)

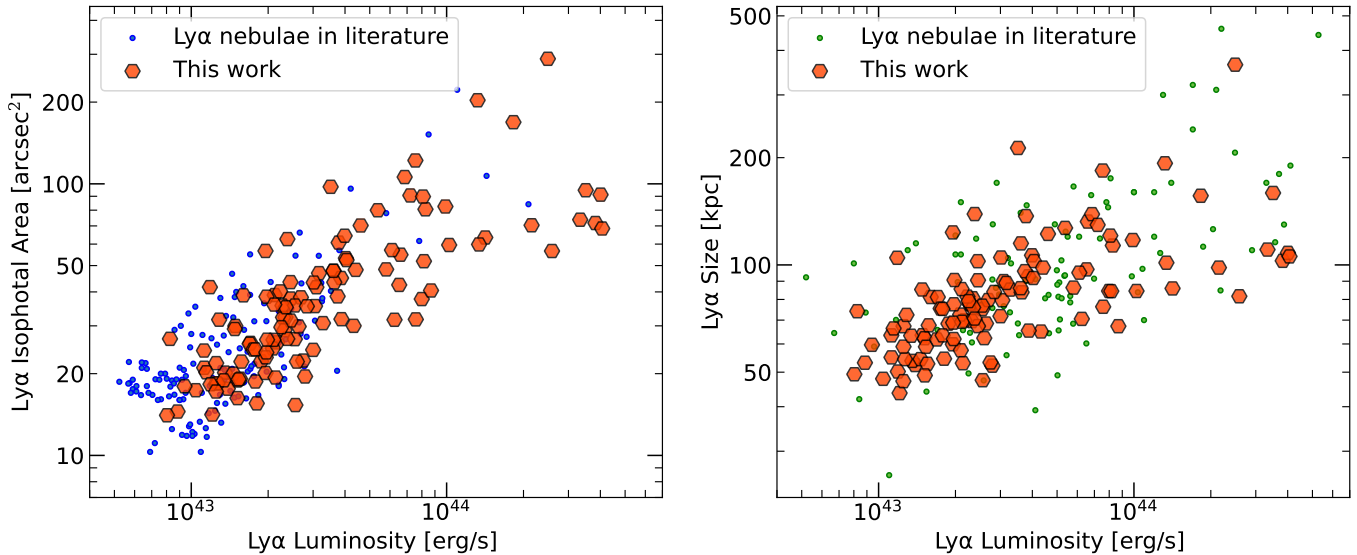


Figure 4. $\text{Ly}\alpha$ isophotal areas (left) and maximum projected sizes (right) versus $\text{Ly}\alpha$ luminosities of the extended $\text{Ly}\alpha$ nebulae in this work compared to other samples from the literature. The comparison samples include LABs, QSO nebulae, and ELANe at $z \simeq 2 - 3$ (e.g., Kikuta et al. 2019; Yang et al. 2010; Arrigoni Battaia et al. 2019; Matsuda et al. 2004, 2011; Borisova et al. 2016; Bădescu et al. 2017; Hennawi et al. 2015; Cantalupo et al. 2014; Cai et al. 2017b). Please check Fig. 6 for further classification of diverse nebula populations.

Besides $\text{Ly}\alpha$, the extended C IV and He II emissions are detected by our observations from the Keck/Cosmic Web Imager (KCWI), indicating the existence of metal-enriched gas on the CGM scale. The multi-wavelength observations and a detailed analysis of Ivory Nebula will be posted in our upcoming paper (Li et al. in prep).

Ivory Nebula is located in the large-scale structure of an LAE overdensity. This structure is confirmed as an overdensity with 12 nebulae (eight bright nebulae with $\text{Ly}\alpha$ luminosity larger than $2.5 \times 10^{43} \text{ erg s}^{-1}$) in the volume of $\simeq 40 \times 20 \times 90 \text{ cMpc}^3$ (Zhang et al. 2024). The bright nebula volume density is comparable and even higher than the well-known protocluster SSA22 (e.g., Steidel et al. 2000; Matsuda et al. 2004).

We also want to emphasize the remarkably close ELAN pair within this overdensity, comprising the Ivory Nebula and MLAN10 as shown in Figure 5. MLAN10 lies approximately 1 arcmin ($\simeq 500 \text{ kpc}$ or 1.6 cMpc at $z = 2.3$) away from the Ivory Nebula with $\text{Ly}\alpha$ luminosity of $8.1 \times 10^{43} \text{ erg s}^{-1}$ and $\text{Ly}\alpha$ extent of 120.8 kpc. We note that MLAN10 is almost located in the projected line along component A and C of the Ivory Nebula, indicating ELANe as nodes of the filamentary cosmic web. We expect that deeper observation can reveal the cosmic-web filaments (Martin et al. 2023; Umehata et al. 2019) probed by relatively bright $\text{Ly}\alpha$ emission bridge (e.g., $\text{SB}_{\text{Ly}\alpha} > 10^{-18} \text{ erg s}^{-1} \text{ cm}^{-2} \text{ arcsec}^{-2}$) and embedded dwarf galaxies connecting the two ELANe.

5. DIVERSE POPULATIONS OF $\text{Ly}\alpha$ NEBULAE

Our sample presents 117 $\text{Ly}\alpha$ nebulae spanning a wide range of properties, e.g., luminosities and sizes. In order to investigate properties of galaxies associated with these nebulae, we cross-match our nebula sample with multi-wavelength observations, which ultimately showcase a diversity of nebulae. In this section, we explore this diversity focusing on multiple diagnostics, including UV fluxes, infrared (IR) fluxes, radio emissions, and AGN activity.

5.1. Type II nebulae missing UV-bright sources

In normal circumstances, the luminous and extended $\text{Ly}\alpha$ emission can be explained by the fluorescence of embedded energetic UV sources (e.g., Cantalupo et al. 2005; Kollmeier et al. 2010; Overzier et al. 2013), including starburst and QSOs. However, we find that the majority of enormous $\text{Ly}\alpha$ nebulae are associated with UV-faint sources. We categorize this intriguing class of enormous $\text{Ly}\alpha$ nebulae as Type II ELAN, defined empirically as enormous $\text{Ly}\alpha$ nebulae ($\gtrsim 100 \text{ kpc}$) lacking any UV-bright source ($M_{\text{UV}} \gtrsim -22$). Oppositely, we define enormous $\text{Ly}\alpha$ nebulae with UV-bright sources ($M_{\text{UV}} \lesssim -22$) as Type I ELANe. The boundary of absolute UV magnitude ($M_{\text{UV}} = -22$) used to differentiate between two types is determined empirically by identifying the critical luminosity where the UV luminosity functions of QSOs and galaxies at $z \sim 2$ intersect (e.g., Shen et al. 2020). The galaxy dominates the faint UV population in $M_{\text{UV}} > -22$ while the QSO dominates the bright UV population in $M_{\text{UV}} < -22$. Because of

Table 2. Properties of Ly α Nebulae

ID	Field	R.A.	Decl.	m_{NB}	m_{g}	A_{iso}	$\log(L_{\text{Ly}\alpha})$	Ly α size	z_{spec}	Comment
		degree	degree	mag	mag	arcsec ²	log[erg s ⁻¹]	kpc		
(1)	(2)	(3)	(4)	(5)	(6)	(7)	(8)	(9)	(10)	(11)
MLAN1	J1349	206.97629	23.96409	22.68	24.08	288.7	44.40	364.7	2.310	T2; <i>Ivory</i>
MLAN2	J0222	35.18785	-2.22342	23.92	25.91	203.2	44.12	192.9		T2
MLAN3	J1349	207.15093	23.9955	22.89	24.55	168.7	44.26	156.3	2.307	T2;R
MLAN4	J1349	206.86169	24.53714	23.43	23.35	121.9	43.88	184.0		T2
MLAN5	J0240	39.93041	-5.99873	24.64	25.58	105.9	43.84	138.8		T2
MLAN6	J0755	119.53963	30.80769	25.47	26.11	97.5	43.55	212.9		T2
MLAN7	J0240	40.49514	-5.70917	19.85	20.35	94.7	44.54	159.2	2.267	Q
MLAN8	J0240	39.95441	-5.32985	19.75	20.35	91.2	44.60	108.1	2.299	Q
MLAN9	J1349	206.98806	24.90205	23.81	24.67	90.6	43.86	129.5		T2
MLAN10	J1349	206.98091	23.9814	23.00	24.77	89.8	43.91	120.8	2.312	T2
...										

NOTE—(1) IDs of Ly α nebulae sorted by the Ly α isophotal area from the largest to the smallest; (2) field name (3-4) coordinates R.A. and Decl. in equinox with an epoch of J2000; (5-6) narrowband (NB387 or NB400) and g-band magnitude; (6-7) isophotal Ly α area and Ly α luminosity above 2σ contour in the unit of arcsec² and erg s⁻¹; (8) projected end-to-end Ly α extent in the unit of physical kpc; (9) spectroscopic redshift if available; (10) comments for the corresponding object (T2: Type II ELAN; R: with radio counterparts; Q: QSO with spectra; IR: IR luminous objects identified by WISE);. Only the first ten sources are listed, and the entire table is available in a machine-readable form in the online journal (now [here](#)).

the the faintness of their UV continuum, it is extremely challenging to reveal Type II ELANe through current QSO and galaxy surveys. In summary, we define two types of enormous Ly α nebulae based on their associated UV sources:

- Type I: These nebulae have associated UV-bright sources ($M_{\text{UV}} \gtrsim -22$), typically QSOs.
- Type II: These nebulae have no detectable UV-bright sources ($M_{\text{UV}} < -22$), typically galaxies, despite their extended and bright Ly α emission.

In our sample, 28 out of 117 ($\simeq 24\%$) nebulae can be identified as enormous Ly α nebulae with projected size over than 100 kpc. Strikingly, 22 of these 28 ELANe ($\simeq 78.6\%$) satisfy the criteria of Type II ELANe, *i.e.*, enormous nebulae missing associated bright UV continuum sources, including the Ivory nebula. It is noteworthy that the Ivory Nebula satisfies the criteria of Type II ELAN, with the UV continuum of component A has been observed with $M_{\text{UV}} = -20.5$ in deep g-band imaging (refer to §4.2 and Fig. 5). We estimate UV magnitude from the continuum flux density following the equation of $M_{\text{UV}} = -2.5 \log(f_{\nu, \text{cont}}) - 48.6 - 5 \log(D_L/10 \text{ pc}) + 2.5 \log(1+z)$, where $f_{\nu, \text{cont}}$ is continuum flux density estimated as shown in § 3.2 and

D_L is the luminosity distance. We regard the brightest target overlapped with the nebula as the associated galaxy except spectroscopic targets. Figure 6 shows the diagram comparing Type II ELAN against other classes including Type I ELAN, QSO nebula, and Ly α blob. We find there is a bimodal distribution of UV magnitude for all ELANe, with Type I ELANe (QSO nebulae) exhibiting bright UV continua and Type II ELANe associated with faint UV fluxes. Note that the UV magnitude valley of this bimodal distribution coincide with the boundary magnitude ($M_{\text{UV}} = -22$) used to differentiate between two types. Our sample shows clearly that the ELAN sample is dominated by Type II with a fraction of $\sim 78.6\%$. Therefore, previous ELAN searches mainly on pre-selected QSOs are highly incomplete (*e.g.*, [Borisova et al. 2016](#); [Arrigoni Battaia et al. 2019](#)).

Besides Ivory Nebula as a typical Type II, we present two other representative Type II nebulae, MLAN2 and MLAN5, in Figure 7. MLAN2 has an extended Ly α emission out to 192.9 kpc with a Ly α luminosity of 1.32×10^{44} erg s⁻¹. Its morphology is nearly circular, with two brighter lobes. MLAN2 exhibits a flat Ly α surface brightness profile of $\simeq 1 - 5 \times 10^{-17}$ erg s⁻¹ cm⁻² arcsec⁻². MLAN5 shows 138.8 kpc filamentary Ly α emission with a luminosity of $6.85 \times$

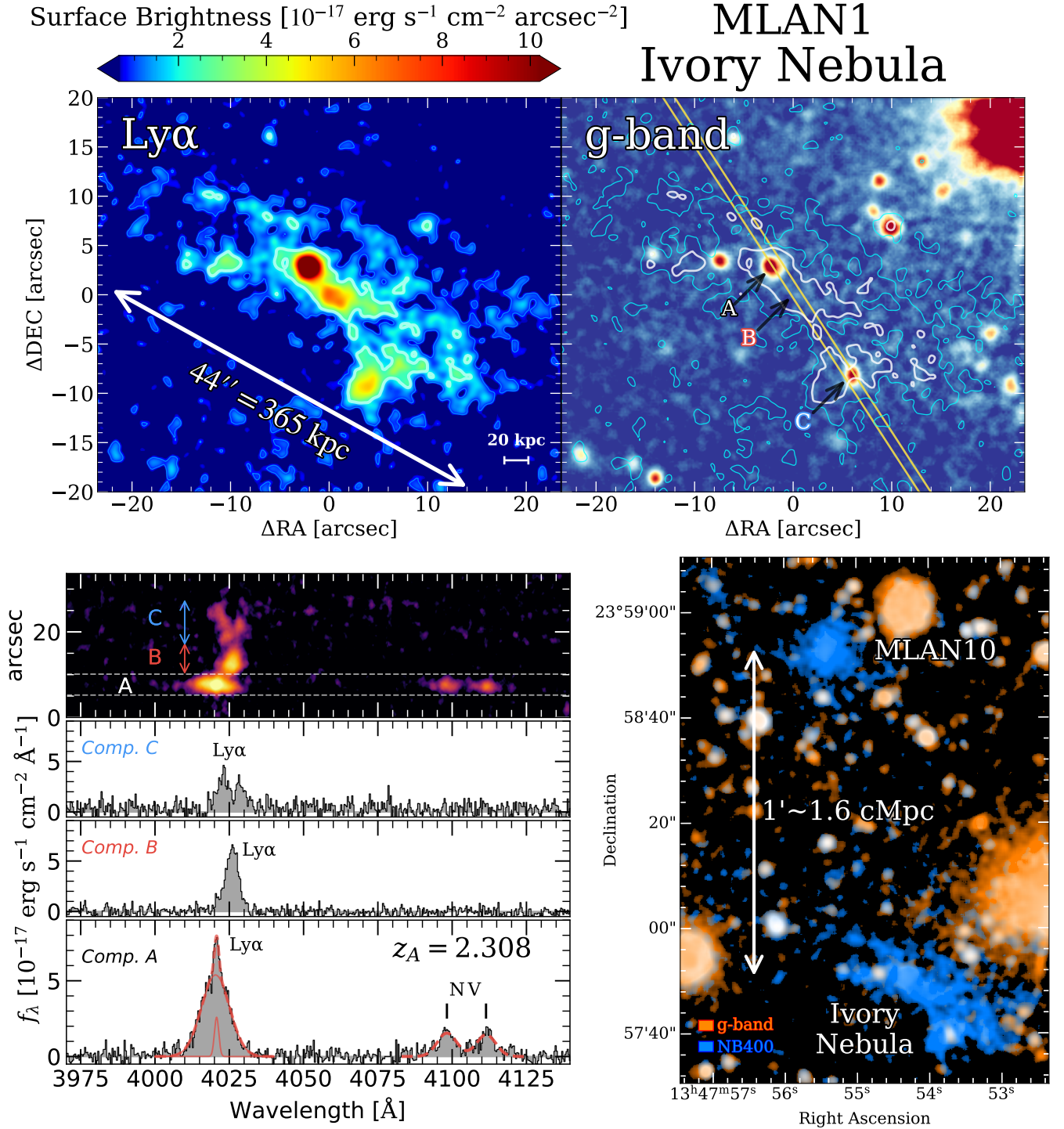


Figure 5. *Upper Panels:* $\text{Ly}\alpha$ line map (left) and g-band image (right) of the field around Ivory Nebula. The line map reveals the extremely extended $\text{Ly}\alpha$ emission of the enormous $\text{Ly}\alpha$ nebula. The 2σ surface brightness limit is $7.76 \times 10^{-18} \text{ erg s}^{-1} \text{ cm}^{-2} \text{ arcsec}^{-2}$. Cyan and white lines represent the 2σ and 5σ $\text{Ly}\alpha$ contours, respectively. Yellow lines denote the long slit to take spectra. *Lower Left Panel:* 2D and 1D spectra of the Ivory Nebula. The 2D spectrum shows the spatial extent of $\text{Ly}\alpha$ emission along the slit (oriented along the yellow lines in the upper right). 1D spectra were extracted using fixed-width apertures corresponding to the three components labeled (component A, B, and C). The spectra reveal complicated $\text{Ly}\alpha$ line profiles and the detection of N V doublet emission in Component A. *Lower Right Panel:* Composite RGB image (g-band in red and NB400 in blue) of the ELAN pair composed of Ivory Nebula and MLAN10. Pixels with values of $< 2\sigma$ RMS are set in black color. The projected angular separation between these two ELANe is about 1 arcmin.

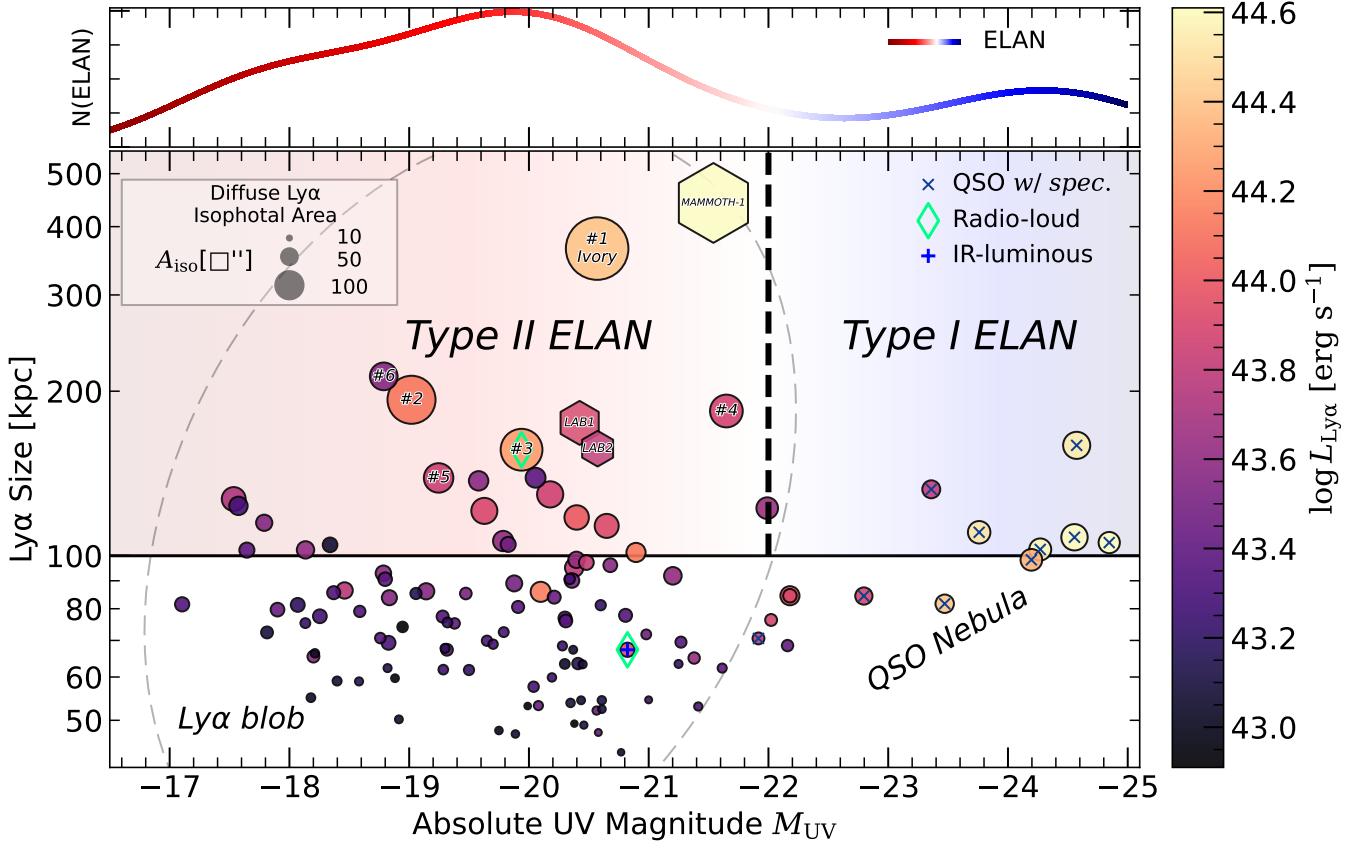


Figure 6. Diagnosis of Type II ELANe, enormous Ly α nebulae (> 100 kpc) with UV-faint ($M_{UV} > -22$) host galaxies. Type II ELANe are the majority ($\sim 80\%$) in the population of enormous Ly α nebulae. The x-axis is the rest-frame absolute UV magnitude. The y-axis denotes the projected Ly α angular size. The size of each circle denotes the diffuse Ly α isophotal area. The color of each circle denotes the Ly α luminosity. The UV magnitude distribution of ELANe is shown in the upper panel with a bimodal feature. Type II ELANe are located in the upper left corner with a faint UV continuum but widespread Ly α emissions, while Type I ELANe are located at the upper right of this figure with a strong UV continuum. The background of this figure is colored just for visual distinction. The largest six nebulae in this work are labeled, which all are Type II nebulae. For summary and comparison, a few Type II nebulae reported in previous literature are drawn as hexagons in this figure, including MAMMOTH-1 (Cai et al. 2017b; Zhang et al. 2023b), SSA22-LAB1, SSA22-LAB2 (Steidel et al. 2000; Matsuda et al. 2004). QSO confirmed by spectroscopic observations (blue cross), radio galaxies (green diamond), and IR-luminous DOGs (blue plus) are overlaid on the figure.

10^{43} erg s^{-1} . The Ly α emission has an emitting core with multiple flux peaks. Despite enormous Ly α structures, no bright UV continuum is detected associated with the nebulae.

The existence of a considerable sample of Type II ELANe poses a puzzle since their large Ly α extent and copious Ly α luminosities could be difficult to explain without copious UV photons. Consequently, additional Ly α powering mechanisms (e.g., gravitational cooling) may play an important role in this category of sources. In fact, the very first discovered blobs (e.g., SSA22 LAB1 and LAB2 in Steidel et al. 2000) and MAMMATH-1 nebula (Cai et al. 2017b) are all Type II ELANe (shown in Fig. 6). The dominance of Type II among ELAN samples shown by our work further high-

lights their importance and demonstrates the universality of these mechanisms. Here we summarize and propose several possible mechanisms to explain these Type II ELANe.

(1) Obscured AGN. The enormous nebulae are illuminated by heavily obscured AGNs. For example, obscured AGNs have been found in the MAMMOTH-1 nebula and SSA22-LAB2, from the X-ray (e.g., Geach et al. 2009; Zhang et al. 2023c) and IR observations (e.g., Arrigoni Battaia et al. 2018b). It is noteworthy that these obscured AGNs are also called Type II AGNs, which can be a possible scenario for powering the Type II ELANe defined in this work. However, it is not expected that each Type II ELAN hosts a Type II AGN. We use the term “Type II” here to emphasize the UV-

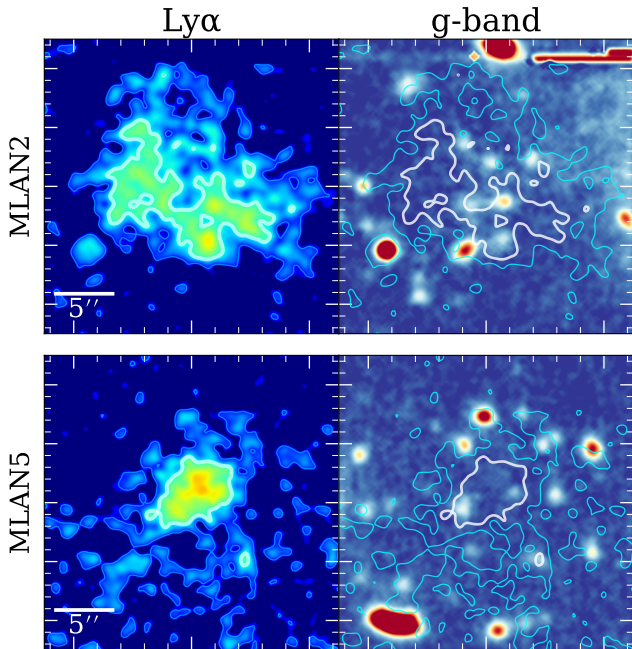


Figure 7. Two representative type II ELANe. The left panels present the smoothed continuum-subtracted $\text{Ly}\alpha$ line maps, and the right panels show the HSC g-band imaging (rest-frame UV). The cyan and white lines represent the 2σ and 5σ $\text{Ly}\alpha$ surface brightness contours. These enormous nebulae are associated with UV-faint sources.

faint properties that can be caused by the dusty nature. In § 5.2, we discuss the mid-infrared properties of our nebulae related to this obscured AGN scenario and corresponding observations in more detail. It is noteworthy that these obscured AGNs are always hosted by dusty starburst galaxies, as shown in the following paragraph.

(2) Dusty starburst. The nebulae may be powered by a dusty starburst that is not detectable in the rest-frame UV due to its dusty nature (*e.g.*, Cen & Zheng 2013). In this scenario, infrared/sub-mm observations using JWST and ALMA could potentially reveal luminous hidden powering sources within the nebulae. For example, SSA22-LAB1 has been confirmed to be composed of numerous sub-millimeter galaxies (SMGs) with violent star formation (*e.g.*, Umehata et al. 2021). It is noteworthy that, for most of Type II ELANe, the $\text{Ly}\alpha$ flux peak tends to be displaced from the flux peak of the galaxy UV continuum (see Fig. 5 and Fig. 7). This phenomenon has been observed before (*e.g.*, Dey et al. 2005) and can be reproduced by starburst model (*e.g.*, Cen & Zheng 2013) by combining complicated effects of galaxy clustering, faint under-resolved sources, and dust. Our observations indicate a tentative ubiquity of this $\text{Ly}\alpha$ peak displacement for Type II ELANe.

(3) Gravitational cooling. The $\text{Ly}\alpha$ emission is due to the cold accretion cooling radiation of filamentary gas onto a massive dark matter halo (*e.g.*, Dijkstra & Loeb 2009; Faucher-Giguère et al. 2010; Haiman et al. 2000; Rosdahl & Blaizot 2012; Daddi et al. 2021). Sensitive sub-millimeter observations could detect cold molecular gas within the halo that may fuel the star formation in the galaxy (Ao et al. 2020). The cooling flow can contribute to the $\text{Ly}\alpha$ at the ongoing stage of massive galaxy formation when there has been a massive dark matter halo in the center (Arrigoni Battaia et al. 2018b; Zhang et al. 2023b).

(4) The relic emission. In this case, the nebula is a relic structure - the UV photons required to power it and $\text{Ly}\alpha$ photons were emitted in the past when the central source was still active. The $\text{Ly}\alpha$ photons can continue scattering in the nebula (*e.g.*, Dijkstra & Loeb 2009; Hayes et al. 2011), even after the central engine shuts off. The most likely central engines powering the original $\text{Ly}\alpha$ emission in this scenario are AGNs with rapid duty cycles (AGN flickering), which can emit copious ionizing radiation that gets converted to $\text{Ly}\alpha$ through recombination (*e.g.*, Schirmer et al. 2016). Resonant $\text{Ly}\alpha$ photons are efficiently stored and will be gradually released, decorrelating from AGN variability on scales of up to 10^6 years depending on the optical depth. After the central engine shuts off, the nebula can continue glowing in $\text{Ly}\alpha$ emission for an extended period due to recombination equilibrium.

(5) Numerous faint interacting galaxies. The nebulae are powered by numerous interacting sources that fall below the detection threshold. A cluster of faint star-forming galaxies or lower-luminosity AGN could fuel the $\text{Ly}\alpha$ fluorescence. The existence of such faint UV sources that cannot be detected individually has been shown through stacking of LAEs (*e.g.*, Kikuta et al. 2023), and it has been demonstrated that they contribute significantly to the extended $\text{Ly}\alpha$ emissions. Further sensitive observations could potentially uncover these hidden power sources within the individual nebulae.

The categorization of Type I and Type II ELANe could be influenced by how UV sources are identified and UV flux measurements are conducted. One factor to consider is the spatial offset that could exist between the $\text{Ly}\alpha$ peak and the UV sources. Typically, only the brightest target within the nebula is taken into account in this work. Consequently, the UV fluxes may appear fainter than they actually are. Moreover, certain emission lines like C IV can enhance the estimate of UV magnitude based on broad-band photometry, leading to measured UV fluxes that appear brighter than they truly

are. Despite these limitations, it is significant that the Type IIs occupy the majority of ELANe.

Type II nebulae represent the most interesting and most important categories of the diverse Ly α nebula population. Note that with only deep NB387/NB400 and g-band imaging observations, detailed mechanisms of these Type II nebulae in our sample are hard to determine. However, the fact that the majority of the Ly α nebula sample is Type II has been clearly shown. Further multi-wavelength follow-up, especially infrared, (sub)mm, and X-ray (*e.g.*, using JWST, ALMA, and Chandra), will be essential for unraveling the power sources and mechanisms. Their study promises to reveal new insights into the interplay between galaxies, supermassive black holes, and CGM in the peak epoch of AGN activity and cosmic star formation.

5.2. Infrared properties of Ly α nebulae

Infrared observations provide key insights into the powering sources of Ly α nebulae, particularly those lacking bright UV/optical counterparts (Type II). Obscured star formation and AGN activity can be revealed in the IR wavelength (*e.g.*, Lyu et al. 2022), which could play an important role in powering extended Ly α emission. In this section, we investigate the mid-infrared properties of our sample.

To analyze the infrared properties of our nebula sample, we cross-matched our 117 nebulae with observations of Wide-field Infrared Survey Explorer (WISE; Wright et al. 2010). WISE surveyed the entire sky at wavelengths of 3.4, 4.6, 12, and 22 μm down to 5σ depths of 0.08, 0.11, 1, and 6 mJy, respectively. For our nebulae at $z \approx 2$, these four WISE bands cover the 1, 1.5, 4, and 7 μm rest-frame wavelength.

The crossmatch results showed WISE detection for 25 out of 117 nebulae ($\approx 21\%$) in at least one band. All these 25 objects are detected in the W1 (3.4 μm) band, with 20, 11, and 4 objects detected in the W2 (4.6 μm), W3 (12 μm), W4 (22 μm) bands respectively. The WISE-detected counterparts of Ly α nebulae have typical AB magnitudes of W1, W2 > 17 . Note that we show all WISE photometry in AB magnitude, which is converted from the Vega magnitude following the relation: $(W1, W2, W3, W4)_{\text{AB}} = (W1, W2, W3, W4)_{\text{Vega}} + (2.699, 3.339, 5.174, 6.620)$.

Among the WISE-detected nebulae, one target (MLAN44) displays an extremely bright flux in the W3 and W4 bands (Fig. 8). The WISE magnitudes of MLAN44 are $m_{3.4\mu\text{m}} = 17.10 \pm 0.10$, $m_{4.6\mu\text{m}} = 14.92 \pm 0.06$, $m_{12\mu\text{m}} = 9.76 \pm 0.04$, and $m_{22\mu\text{m}} = 7.12 \pm 0.08$ in Vega magnitude. MLAN44 is the most mid-IR luminous source in our sample, despite having a faint UV counter-

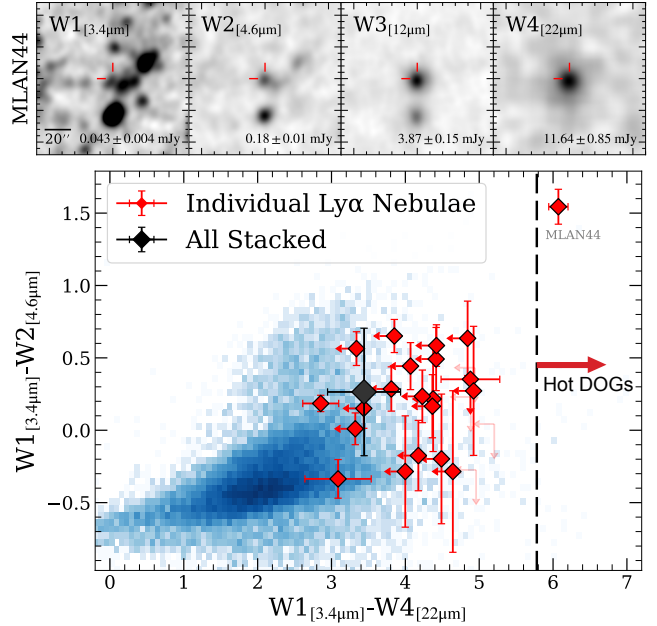


Figure 8. Upper: Cutout images of MLAN44 in the WISE W1 (3.4 μm), W2 (4.6 μm), W3 (12 μm), and W4 (22 μm) bands, from left to right. The cutout size is $2' \times 2'$. Lower: The WISE infrared color-color diagram of the matched and stacked sources in our sample. The blue-indexed 2D histogram denotes the distribution of sources with < 0.3 mag errors in W1 (3.4 μm), W2 (4.6 μm), and W4 (22 μm) in the all-sky release catalog with Galactic latitude $b > 40^\circ$. Objects to the right of the dashed line are hot dust-obscured galaxies (Eisenhardt et al. 2012).

part ($m_g = 23.76 \pm 0.02$). The extended Ly α emission around MLAN44 reaches 67 kpc in projection with a luminosity of $L_{\text{Ly}\alpha} = 8.69 \times 10^{43} \text{ erg s}^{-1}$. The extreme infrared colors and luminosity, combined with the spatial extent and high Ly α luminosity, suggest that MLAN44 hosts an obscured AGN or dusty starburst that likely powers the Ly α emission through photo-ionization.

MLAN44 represents one case of the luminous infrared galaxy (LIRGs), a class of objects identified by their high infrared luminosity and faint optical counterparts (*e.g.*, Dey et al. 2008; Wu et al. 2012; Eisenhardt et al. 2012; Liu et al. 2022). In nature, these galaxies are explained by the dust-obscured violent starburst called dust-obscured galaxy (DOG) or obscured AGN activity (hot DOG or Type-II QSO). In this work, we do not make specific distinctions, and refer to them collectively as (hot) DOGs. The WISE colors and luminosities of MLAN44 are consistent with known hot DOGs ($W1-W4 \lesssim 5.8$) at similar redshifts (*e.g.*, Ishikawa et al. 2023). Mid-IR imaging for hot dust and spectroscopy targeting polycyclic aromatic hydrocarbon (PAH) emission features can help distinguish the contributions from AGN activity and star formation (Colbert et al. 2011).

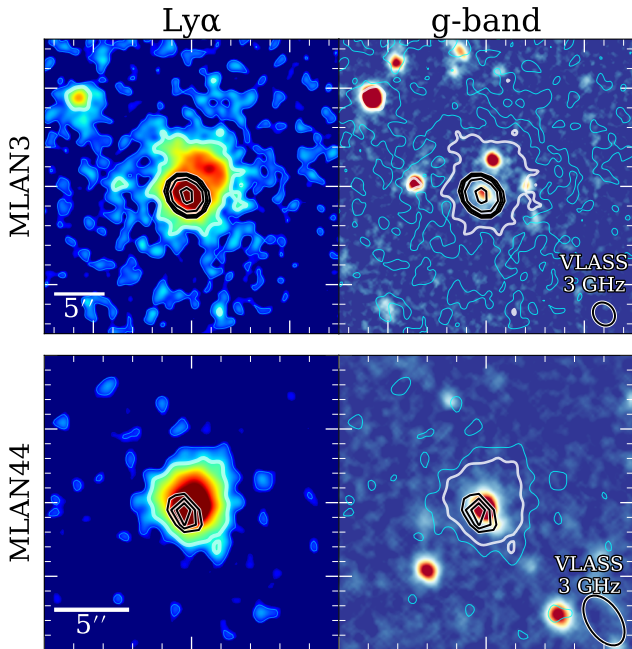


Figure 9. Two $\text{Ly}\alpha$ nebulae with radio counterparts. The left panels present the smoothed continuum-subtracted $\text{Ly}\alpha$ line maps, and the right panels show the HSC g-band imaging. The cyan and white lines represent the 2σ and 5σ $\text{Ly}\alpha$ surface brightness contours. VLA 3 GHz radio observations from VLASS are overlaid as black contours of 5, 6, 7, 10, 20 where $\sigma = 0.15$ mJy.

The JWST MIRI observations are expected for this population of $\text{Ly}\alpha$ nebulae to unravel the dusty nature and examine the powering mechanism of the source.

Despite the obscured nature, almost all hot DOGs have $\text{Ly}\alpha$ emission and are detected as $\text{Ly}\alpha$ emitters (Bridge et al. 2013). Furthermore, a significant fraction of hot DOGs exhibit $\text{Ly}\alpha$ nebulae extending to scales of > 30 kpc, well beyond the dust envelopes (e.g., Bridge et al. 2013; Dey et al. 2005). However, with the detection limit of WISE, only the most luminous infrared galaxies can be detected. The fraction of nebulae with WISE-detected luminous IR counterparts can be estimated to be $1/117 \sim 0.9\%$ with a number density of 1.14×10^{-7} cMpc $^{-3}$. This indicates the extremely low number density of $\text{Ly}\alpha$ nebulae with hot DOGs. More sensitive mid-IR and Far-IR/sub-millimeter observations can better reveal the dust-obscured nature.

5.3. $\text{Ly}\alpha$ Nebulae associated with Radio Galaxies

The first extended $\text{Ly}\alpha$ nebulae were discovered around HzRGs and radio quasars (e.g., McCarthy et al. 1987), highlighting the diversity of radio properties early on. The interaction of relativistic jets from central SMBHs with ambient gas is believed to contribute to powering and distributing $\text{Ly}\alpha$ emission on large scales

(e.g., McCarthy 1993). However, owing to the small sample sizes of $\text{Ly}\alpha$ nebulae and the fact that powerful radio sources are found only in a very small fraction of high- z galaxies, very few $\text{Ly}\alpha$ nebulae have radio counterparts. In this section, we compile the public radio survey to quantify the radio properties of our nebula sample.

We match our 117 nebulae with public data archives of radio observations, including the VLA Faint Images of the Radio Sky at Twenty-Centimeters (FIRST) Survey (White et al. 1997; Helfand et al. 2015), the NRAO VLA Sky Survey (NVSS, Condon et al. 1998), VLA Sky Survey (VLASS, e.g., Lacy et al. 2020), and TIFR GMRT Sky Survey (TGSS, Intema et al. 2017). These four surveys cover all eight fields in our work. With the matching radius of $10''$, two nebulae (MLAN3 and MLAN44, shown in Figure 9) have radio counterparts in the imaging data of these four surveys.

The VLASS, FIRST/NVSS, and TGSS surveys capture the radio emission at 3.0 GHz, 1.4 GHz, and 150 MHz, respectively. At a depth of FIRST (flux limits of ~ 1 mJy), the 115 non-detections place upper limits on the 1.4 GHz radio luminosities of our sample at $\lesssim 4 \times 10^{25}$ W Hz $^{-1}$. For the two nebulae with radio detections, MLAN3 has a 1.4 GHz peak flux density of 10.85 ± 0.15 mJy in FIRST and 11.9 ± 0.5 mJy in NVSS. MLAN44 has a lower 1.4 GHz peak flux of 2.71 ± 0.13 mJy in FIRST and 4.5 ± 0.5 mJy in NVSS. At 3 GHz, VLASS measures flux densities of 4.62 ± 0.14 mJy and 1.30 ± 0.13 mJy for MLAN3 and MLAN44, respectively. In the lower frequency TGSS 150 MHz first alternative data release (ADR1), the sources have peak fluxes of 55.3 ± 6.8 mJy (MLAN3) and 25.9 ± 4.3 mJy (MLAN44). Combining these multi-frequency measurements, we can derive radio spectral indices. Adapting values from de Gasperin et al. (2018) that matched sensitivity and resolution across the surveys, the best-fit spectral indices are -0.80 ± 0.09 for MLAN3 and -0.81 ± 0.17 for MLAN44.

As revealed by previous studies (e.g., Villar-Martín et al. 2007; Shukla et al. 2021; Wang et al. 2023), $\text{Ly}\alpha$ nebulae appear to be nearly ubiquitous around HzRGs, implying a $\sim 100\%$ $\text{Ly}\alpha$ nebulae detection rate for HzRGs. The prevalence of $\text{Ly}\alpha$ nebulae around HzRGs is explained by their gas-rich environments and AGN activity, both of which are conducive to powering and scattering copious $\text{Ly}\alpha$ photons on large scales. The shock-induced radiation powered by radio jets and fluorescent $\text{Ly}\alpha$ emission attributed to photo-ionization by central AGNs can dominate for these $\text{Ly}\alpha$ nebulae with radio-loud counterparts.

However, the situation changes when turning the argument around. Only two out of 117 ($\simeq 2\%$) nebulae in

our sample have radio counterparts, corresponding to a total volume density of $2.3 \times 10^{-7} \text{ cMpc}^{-3}$. The low fraction of the powerful radio galaxies associated with Ly α nebulae implies that radio galaxies are not frequently responsible for the extended luminous nebulae. Numerous previous LAB surveys (*e.g.*, Matsuda et al. 2004; Yang et al. 2009; Kikuta et al. 2019) have shown that the majority of Ly α nebulae have radio-quiet natures. In summary, HzRGs can be a subset of the whole Ly α nebula sample.

Despite the rarity of radio-loud Ly α nebulae in our sample, it is noteworthy that we find an excess in the nebula number density for the two fields J0240 and J1349 that host the radio-detected nebulae. The number densities are $1.70 \times 10^{-5} \text{ cMpc}^{-3}$ in the J0240 field and $2.60 \times 10^{-5} \text{ cMpc}^{-3}$ in the J1349 field, a factor of $\sim 2.5\text{--}4\times$ higher than the average LAB number density at $z=2.3$ (*e.g.*, Yang et al. 2010). Note that this nebula density excess is averaged in a vast cosmological volume of $\sim 150 \times 150 \times 90 \text{ cMpc}^3$. This tentatively suggests a correlation between the presence of radio-loud Ly α nebulae and large-scale Ly α nebula overdensities. On the other hand, radio-loud Ly α nebulae could be related to the existence of ELANe. Among the 28 ELANe in our sample, 18 ($\sim 64\%$) are located in the J0240 and J1349 fields. Although it is well known that both HzRGs and Ly α nebulae trace the proto-clusters at high redshift (*e.g.*, Mayo et al. 2012; Dannerbauer et al. 2014; Matsuda et al. 2004; Venemans et al. 2007; Yang et al. 2010; Bădescu et al. 2017; Zhang et al. 2024), not all galaxy overdensities have ELANe or a large group of Ly α nebulae. There are some invisible additional parameters affecting the illumination of Ly α nebulae.

One possible invisible parameter is the gas environment of neutral Hydrogen (H I) in the IGM. The gas-rich environment could simultaneously promote the young radio galaxy and Ly α nebulae. This could lead to the observation that radio galaxies are often found in the centers of assembling protoclusters, as progenitors of local giant central cluster galaxies (*e.g.*, Hatch et al. 2009; Wylezalek et al. 2013). Therefore, it is possible that radio source are predominantly found in the largest Ly α overdensities (*e.g.*, Kurk et al. 2000; Pentericci et al. 2000). Furthermore, Ly α nebulae and ELANe tends to live in these galaxy overdensities (*e.g.*, Steidel et al. 2000; Dey et al. 2005; Matsuda et al. 2005; Prescott et al. 2009; Cai et al. 2017b; Arrigoni Battaia et al. 2018a). Therefore, while rare overall, these giant radio-loud Ly α nebulae could be effective tracers of the massive overdensities with a number excess of Ly α nebula and the emergence of ELANe in the large-scale structure. Further studies of larger samples are still needed

Table 3. Measured fluxes of stacked nebulae

Filter Band	Flux Density f_ν [μJy]
HSC g	$1.22 \pm 0.26^\dagger$
WISE W1 3.4 μm	29 ± 8
WISE W2 4.6 μm	37 ± 11
WISE W3 12 μm	286 ± 32
WISE W4 22 μm	690 ± 250
VLA S 2-4GHz	19 ± 6

† AB magnitude $m_g = 23.68 \pm 0.23$.

to solidify the connection between radio-loud galaxies, nebula overdensities, and protocluster environments.

Except for the all-sky radio survey, we further cross-match our sample with the Low-Frequency Array (LOFAR) Two-metre Sky Survey (LoTSS), which can detect fainter radio sources at the low-frequency radio band (Shimwell et al. 2022). However, the public LoTSS DR2 data release currently only covers two of our fields (J1349 and J0755). Four nebulae (MLAN3, MLAN25, MLAN16, and MLAN63) in these two fields have radio counterparts in the LoTSS imaging. With the exception of MLAN3, the other three galaxies have relatively faint fluxes ($< 1 \text{ mJy}$ at 150 MHz), below the detection limit of the four radio surveys we matched.

It is noteworthy that LOFAR imaging reveals giant radio lobes of MLAN3. This system represents one of the first samples of giant double-lobed radio galaxies associated with enormous Ly α nebulae at high- z . Please refer to our upcoming work (Li et al. in prep) for a detailed analysis of this target.

5.4. Existence of active galactic nuclei

Despite the fact that detailed Ly α powering mechanisms are still debated, there is a consensus that the role of AGN is not negligible, especially for the brightest Ly α nebulae (Geach et al. 2009). However, except for the ultra-luminous broad-line QSO, it is challenging to identify AGNs unambiguously, especially for our high redshift sample. In this section, we discuss the emergence of AGN in our nebula sample.

A few approaches can reveal the presence of an AGN. The most robust evidence is X-ray detection. We checked for X-ray counterparts to our nebula sample using the XMM-Newton Serendipitous Source Catalogue (Webb et al. 2020) and Chandra Source Catalog (Evans et al. 2010). Because our survey fields were newly targeted, no deep X-ray observation covered them. Only

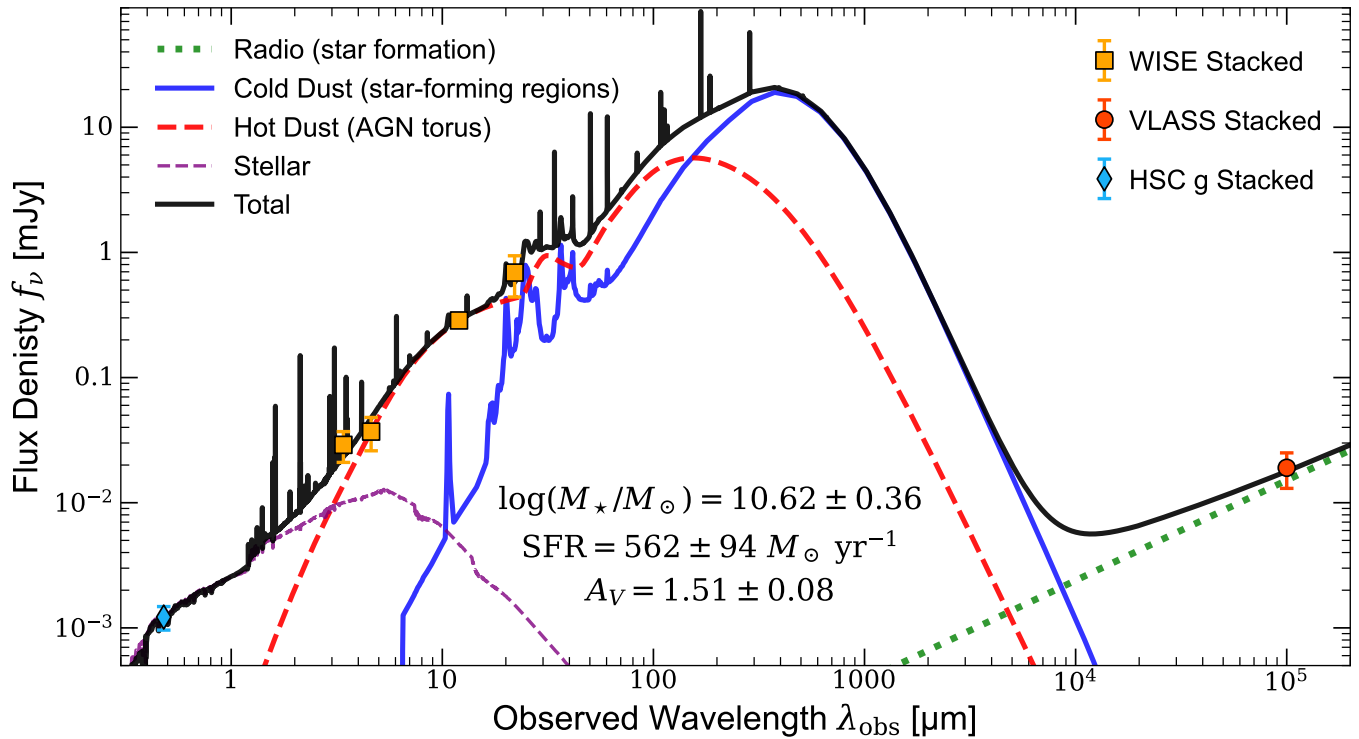


Figure 10. Spectral energy distribution (SED) for the average source powering Ly α nebulae by stacking all 117 targets in this work. The observed data are from stacking of our Subaru/HSC g-band imaging (blue diamond), WISE imaging (orange squares), and VLASS S-band imaging (red circle). The black line denotes the best fit of CIGALE, together with the individual components: hot dust emission (red dashed line), cold dust emission (blue line), stellar emission (purple dashed line), and the radio emission from star formation (green dotted line). The best-fit galaxy stellar mass, SFR, and dust attenuation are annotated in the figure.

partial overlap exists for fields J0222 and J0210, but no X-ray counterparts were detected for any of our nebulae in either catalog. Radio emissions can also act as evidence of AGN activity, despite only a small fraction of AGN is radio-loud, probably due to a short duty cycle of the radio-loud phase (*e.g.*, Tadhunter 2016). As the section 5.3 presents, two nebulae (MLAN3 and MLAN44) have mJy-level radio counterparts. Also note that MLAN44 has extremely bright mid-IR fluxes, indicating a dust-obscured AGN’s existence.

Emission line properties from spectroscopy can help identify the emergence of AGN. We can estimate an unbiased AGN fraction in our sample based on our spectroscopic follow-up, which requires no prior knowledge of the AGN activity. Out of seven confirmed nebulae (Figure 3), five show AGN features (broad C IV lines for MLAN14, MLAN64, and MLAN84; highly ionized N V lines for MLAN1; radio galaxy for MLAN3). This implies an AGN fraction of $5/7 \simeq 71\%$. Moreover, our sample also includes QSOs targeted by spectroscopic surveys. Among the 117 nebulae in our sample, eight (MLAN7, MLAN8, MLAN14, MLAN16, MLAN18, MLAN27, MLAN28, and MLAN31) have

been surveyed and confirmed as QSOs by SDSS (Lyke et al. 2020).

5.5. Understanding the Observed Diversity: Manifestations of Massive Galaxy Evolution

The population of Ly α nebulae displays a remarkable diversity in their observed multi-wavelength properties. By synthesizing the observations across the multiple wavebands, we unravel the intricate natures of nebulae and associated galaxies. Despite this diversity, there is supposed to be an overarching picture of galaxy evolution driving the emergence of extended Ly α nebulae. In this section, we aim to understand the observed diversity of Ly α nebulae under the framework of massive galaxy formation and evolution.

In order to gain an average view of host galaxies of Ly α nebulae, we stack imaging data in the rest-frame UV (Subaru/HSC g-band), IR (WISE W1,W2,W3,W4), and radio (VLASS S-band) wavelengths. We stack the cutout images of all sources by clipping the 3σ outliers and taking the mean on the pixel scale. These bands can trace key properties including dust attenuation, star formation rate, and AGN activity. The stacked imaging of

all these bands show $> 2\sigma$ signals. The measured fluxes are listed in Table 3. Note that we test the stacking by removing QSOs, radio galaxies, or dust-obscured galaxies (MLAN44), which give the same results as the stacking of the full sample to within 1σ . Therefore, aiming to get the average property of Ly α nebulae, we include all 117 sample sources in the stacking process.

We run spectral energy distribution (SED) fitting for the stacked source using CIGALE, which is a Python-based code to efficiently model the X-ray to radio spectrum of galaxies with AGN and estimate their physical properties such as star formation rate, attenuation, and stellar mass (Boquien et al. 2019; Yang et al. 2022). For CIGALE modeling, we assume a delayed- τ star-formation history, where an optional late starburst is allowed in the last 20 Myr. We use Bruzual & Charlot (2003) stellar population synthesis models and a broad ionization parameter range of -1.0 to -3.0. We adopt a modified Calzetti et al. (2000) attenuation curve, which allows the variation of the power-law slope by ± 0.3 . We use the dust emission templates of Dale et al. (2014) and AGN models from Stalevski et al. (2012, 2016). Besides, galaxy synchrotron and AGN radio emissions are included.

The best-fit model and physical properties are presented in Fig. 10. The SED reveals a massive galaxy ($\log M_*/M_\odot = 10.62 \pm 0.36$) with copious dust ($A_V = 1.51 \pm 0.08$), violent star formation (SFR=562 \pm 94 $M_\odot \text{ yr}^{-1}$), and obscured AGN. This clearly shows the dusty nature of the host galaxy associated with the Ly α nebula. The dusty nature of galaxies associated with Ly α nebulae implies that copious Ly α photons and UV photons can escape from the dusty galaxies to the CGM scale. While the obscuration makes Ly α and UV escape difficult, some can surely escape from dusty galaxies through mechanisms such as geometric (anisotropic escape), kinematic (wind dispersal), and radiative transfer effects. Otherwise, luminous *in-situ* Ly α emissions are needed in the CGM. Further studies are expected to resolve this puzzle of luminous Ly α nebulae around dusty galaxies.

Synthesizing multi-wavelength observations, we propose that Ly α nebulae can represent a general manifestation during the key phase of massive galaxy assembly. The diverse population of Ly α nebulae, therefore, provides a window into the intricate life cycles of massive galaxies emerging from dust during the peak epoch of galaxy assembly (*e.g.*, Hopkins et al. 2008). Early in the starburst stage, galaxies undergo intense dust-obscured starburst activity, and energetic AGN turn on at the galaxy center driving large-scale gas flow and powering extended Ly α nebulae. This dusty phase dominates the

time scale and represents an average powering source as shown by our SED fitting of stacked Ly α nebulae (Fig. 10). As the galaxies evolve, they will experience a very short-time “blowout” phase, possibly observed as radio-loud galaxies. Further, with the copious dust and gas exhausted and expelled, the QSO will be bare and then decay. The small fraction of radio galaxy ($\lesssim 2\%$) and QSO ($\lesssim 7\%$) can be well explained by the short time scale at these stages. The majority ($\sim 80\%$) of enormous Ly α nebulae is Type II, whose galaxies are hidden in dust and UV-faint, with violent starburst ongoing and possible obscured AGN shining. Further, the dominant dusty nature of Ly α nebula shown by our stacked results proves that a long dusty lifetime occurs when the massive galaxies undergo violent starburst and black hole assembly. In the future, IR and (sub)mm observations (*e.g.*, JWST and ALMA) for the discovered Ly α nebulae and Ly α observations for dusty starburst galaxies and obscured AGNs at high- z would be critical for disentangling the histories of individual systems and piecing together an overarching picture of massive galaxy formation and evolution at the cosmic noon.

6. SUMMARY

We have carried out wide-field, deep imaging observations of eight fields selected by the MAMMOTH approach at $z = 2.18$ and $z = 2.29$ using Subaru/HSC. We select 117 Ly α nebulae in an unbiased way and compile multi-wavelength data from UV to radio to achieve a panchromatic perspective on the properties of Ly α nebulae. An observed diversity of nebula population has been revealed. The main conclusions are summarized as follows:

1. Searching over 12 deg², we discover 117 Ly α nebulae with luminous ($L_{\text{Ly}\alpha} = 8 - 40 \times 10^{43} \text{ erg s}^{-1}$) and extended (40 - 400 kpc) Ly α emissions. Among the sample, 28 nebulae have Ly α sizes larger than 100 kpc and are labeled as enormous Ly α nebulae (ELANe). We confirm the redshifts of seven nebulae spectroscopically, with an AGN fraction ($\gtrsim 71\%$) indicated by broad emission lines and high-ionization emission lines.
2. An intergalactic nebula, dubbed the Ivory Nebula, is highlighted with extended filamentary and well-resolved clumpy Ly α emission between two galaxies. The Ivory Nebula has a Ly α luminosity of $L_{\text{Ly}\alpha} = 2.5 \times 10^{44} \text{ erg s}^{-1}$ and an end-to-end angular extent of $44.4'' \simeq 365 \text{ kpc}$. The extreme properties make it one of the largest nebulae discovered in the Universe and provide an opportunity to directly study gas flow in galaxy formation.

3. We present an observed diversity of $\text{Ly}\alpha$ nebula multi-wavelength properties. There is a bimodal distribution for UV magnitude of powering galaxies. UV-faint sources ($M_{\text{UV}} > -22$) dominate the population of enormous $\text{Ly}\alpha$ nebulae with size > 100 kpc. This intriguing class of $\text{Ly}\alpha$ nebulae is categorized as Type II ELAN. Type II ELANe constitute the majority of enormous nebulae in the universe but remain largely hidden in all-sky surveys. Dusty starburst and obscured AGN activity can help to resolve the puzzle.
4. A small fraction of $\text{Ly}\alpha$ nebulae have very luminous IR counterparts ($\sim 1\%$ $W_{424\mu\text{m}} > 5$ mJy) and radio galaxy counterparts ($\sim 2\%$). About 7% $\text{Ly}\alpha$ nebulae are associated with QSOs. Radio galaxy nebulae could trace a nebula-rich large-scale environment. Out of 28 ELANe in our sample, 18 ($\sim 64\%$) are located in the J0240 and J1349 fields, where two radio nebulae reside.
5. The SED of stacked $\text{Ly}\alpha$ nebulae reveal a massive ($\log M_*/M_\odot = 10.62 \pm 0.36$), dusty ($A_V = 1.51 \pm 0.08$), star-forming ($\text{SFR} = 562 \pm 94 M_\odot \text{ yr}^{-1}$) galaxy with an obscured AGN activity.

We propose a model where the diverse $\text{Ly}\alpha$ nebula categories capture massive galaxies at different evolutionary stages as they are violently assembling. A relatively long dusty stage has been suggested by the majority of Type II ELANe and dusty nature of stacked SED. In this stage, violent star formation and obscured AGN can play a role in powering the circumgalactic $\text{Ly}\alpha$ nebulae. In conclusion, we collect a large sample of $\text{Ly}\alpha$ nebulae and underscore the pivotal role of $\text{Ly}\alpha$ nebulae in understanding the intricate processes governing galaxy formation and evolution at high- z . In the future, more infrared observations, such as those from the James Webb Space Telescope (JWST) and the Atacama Large Millimeter/submillimeter Array (ALMA), will be vitally needed for studying the discovered $\text{Ly}\alpha$ nebulae. Additionally, observing $\text{Ly}\alpha$ emissions of more dusty starburst galaxies and obscured AGNs at high- z in an unbiased way will be essential for unraveling the physical processes of these systems. Together, these efforts will paint an overarching picture of the formation and evolution of massive galaxies during the cosmic noon.

ACKNOWLEDGMENTS

M.Li, Z.Cai, Y.Wu, S.Zhang, and B.Wang acknowledge support from the National Key R&D Program of China (grant no. 2023YFA1605600), the National Science Foundation of China (grant no. 12073014),

the science research grants from the China Manned Space Project with No. CMS-CSST-2021-A05, and Tsinghua University Initiative Scientific Research Program (No. 20223080023). SC gratefully acknowledges support from the European Research Council (ERC) under the European Union’s Horizon 2020 Research and Innovation programme grant agreement No 864361.”

This research is based in part on data collected by Hyper Suprime-Cam at the Subaru Telescope, which is operated by the National Astronomical Observatory of Japan. We are honored and grateful for the opportunity of observing the Universe from Maunakea, which has the cultural, historical, and natural significance in Hawaii. The authors wish to recognize and acknowledge the very significant cultural role and reverence that the summit of Maunakea has always had within the indigenous Hawaiian community. We are most fortunate to have the opportunity to conduct observations from this mountain. The Hyper Suprime-Cam (HSC) collaboration includes the astronomical communities of Japan, Taiwan, and Princeton University. The HSC instrumentation and software were developed by the National Astronomical Observatory of Japan (NAOJ), the Kavli Institute for the Physics and Mathematics of the Universe (Kavli IPMU), the University of Tokyo, the High Energy Accelerator Research Organization (KEK), the Academia Sinica Institute for Astronomy and Astrophysics in Taiwan (ASIAA), and Princeton University. Funding was contributed by the FIRST program from Japanese Cabinet Office, the Ministry of Education, Culture, Sports, Science and Technology (MEXT), the Japan Society for the Promotion of Science (JSPS), Japan Science and Technology Agency (JST), the Toray Science Foundation, NAOJ, Kavli IPMU, KEK, ASIAA, and Princeton University.

This paper makes use of software developed for the Large Synoptic Survey Telescope. We thank the LSST Project for making their code available as free software at <http://dm.lsst.org>

This paper makes use of data from PS1. The Pan-STARRS1 Surveys (PS1) have been made possible through contributions of the Institute for Astronomy, the University of Hawaii, the Pan-STARRS Project Office, the Max-Planck Society and its participating institutes, the Max Planck Institute for Astronomy, Heidelberg and the Max Planck Institute for Extraterrestrial Physics, Garching, The Johns Hopkins University, Durham University, the University of Edinburgh, Queen’s University Belfast, the Harvard-Smithsonian Center for Astrophysics, the Las Cumbres Observatory Global Telescope Network Incorporated, the National Central University of Taiwan, the Space Telescope Sci-

ence Institute, the National Aeronautics and Space Administration under Grant No. NNX08AR22G issued through the Planetary Science Division of the NASA Science Mission Directorate, the National Science Foundation under Grant No. AST-1238877, the University of Maryland, and Eotvos Lorand University (ELTE) and the Los Alamos National Laboratory.

This publication makes use of data products from the Wide-field Infrared Survey Explorer, which is a joint project of the University of California, Los Angeles, and the Jet Propulsion Laboratory/California Institute of Technology, funded by the National Aeronautics and Space Administration.

This paper includes data gathered with the 6.5-meter Magellan Telescope located at Las Campanas Observatory, Chile.

APPENDIX

A. APPROACH TO ESTIMATE THE LINE FLUX FROM TWO-BAND OBSERVATIONS

In this appendix, we delineate the methodology for calculating the flux of emission lines and the continuum from multi-band imaging data.

We first characterize the basic notation and definition. The intrinsic spectral energy distribution of an astrophysical source as the radiative flux density per unit frequency or wavelength interval is described by f_ν or f_λ , expressed in ν -units ($\text{erg cm}^{-2} \text{s}^{-1} \text{Hz}^{-1}$) and λ -units ($\text{erg cm}^{-2} \text{s}^{-1} \text{\AA}^{-1}$), respectively. These two representations are related through:

$$f_\nu d\nu = f_\lambda d\lambda \quad ; \quad c = \lambda\nu \quad ; \quad \left| \frac{d\nu}{d\lambda} \right| = \frac{c}{\lambda^2},$$

where c is the speed of light in vacuum.

Photometric measurements typically utilize photometric filters that probe the flux density over defined wavelength intervals or passbands (*e.g.*, Bessell 1990; Fukugita et al. 1996). Photometric filters are defined by their transmission curves $T_x(\lambda)$, which describe their response as a function of wavelength. For convenience, we use $T_x(\lambda)$ to present the total system response including atmospheric transmission, the throughput of the telescope, the instrument, the quantum efficiency of the detector, the filter response function, and any other response. All photons received within a given pass-band during the measuring process get integrated, hence the wavelength distribution of f_λ are lost. For this reason, the flux of a source measured in a given filter “x” is effectively defined as the average flux density in the pass-band weighted by the filter transmission curve. For photon-counting detectors like CCDs, The number of photoelectrons per second detected by filter “x” from a source with an intrinsic spectral energy distribution $f_\lambda(\lambda)$ is

$$N_p = \int f_\lambda(\lambda) T_x(\lambda) / h\nu d\lambda = \frac{1}{hc} \int \lambda f_\lambda(\lambda) T_x(\lambda) d\lambda, \quad (\text{A1})$$

where $T_x(\lambda)$ is the total system response. If $f_\lambda(\lambda)$ and $T_x(\lambda)$ are both continuous and $T_x(\lambda)$ is nonnegative over the wavelength interval, then from equation (A1) and the Mean Value Theorem for Integrals there exists a λ_{iso} such that $f_\lambda(\lambda_{\text{iso}}) \int \lambda T_x(\lambda) d\lambda = \int \lambda f_\lambda(\lambda) T_x(\lambda) d\lambda$. Thus we obtain

$$\langle f_\lambda \rangle_x = f_\lambda(\lambda_{\text{iso}}) = \frac{\int f_\lambda T_x \lambda d\lambda}{\int T_x \lambda d\lambda}, \quad (\text{A2})$$

where λ_{iso} denotes the “isophotal wavelength” and $\langle f_\lambda \rangle_x$ denotes the **mean flux density** measured by filter band “x”.

We can describe equation (A1) in terms of frequency. Note that $d\lambda/\lambda = d\nu/\nu$ and $f_\lambda = f_\nu \frac{c}{\lambda^2}$. Thus we have

$$N_p = \frac{1}{hc} \int \lambda f_\lambda(\lambda) T_x(\lambda) d\lambda = \frac{1}{h} \int f_\nu(\nu) T_x(\nu) d\nu/\nu. \quad (\text{A3})$$

Similar to the derivation given by equation (A2), we can also define the mean flux density in ν -units:

$$\langle f_\nu \rangle_x = \frac{\int f_\nu T_x \frac{d\nu}{\nu}}{\int T_x \frac{d\nu}{\nu}} = \frac{\int f_\lambda T_x \lambda d\lambda}{c \int T_x \frac{d\lambda}{\lambda}}. \quad (\text{A4})$$

For consistency of conversion, we need a wavelength $\lambda_{\text{pivot},x}$ to make

$$\langle f_\nu \rangle_x = \frac{\lambda_{\text{pivot},x}^2}{c} \langle f_\lambda \rangle_x. \quad (\text{A5})$$

We obtain

$$\lambda_{\text{pivot},x} = \sqrt{\frac{\int T_x \lambda \, d\lambda}{\int T_x \frac{d\lambda}{\lambda}}}. \quad (\text{A6})$$

The $\lambda_{\text{pivot},x}$ is known as the **pivot wavelength** of filter band “x” (e.g., Koornneef et al. 1986; Tokunaga & Vacca 2005). The pivot wavelength provides an exact relation between $\langle f_\nu \rangle_x$ and $\langle f_\lambda \rangle_x$ by equation (A5). For convenience, we denote $\langle \lambda^\alpha \rangle_x = \int \lambda^\alpha T_x \, d\lambda / \int T_x \, d\lambda$. Hence the pivot wavelength can be written as $\lambda_{\text{pivot},x} = \sqrt{\langle \lambda \rangle_x / \langle \lambda^{-1} \rangle_x}$.

We assume the spectral energy distribution of a line-emitting sources is a power-law continuum plus a delta function emission line:

$$f_\lambda = f_{\lambda,\text{cont}} + f_{\lambda,\text{line}} = f_0(\lambda/\lambda_0)^\beta + F_{\text{line}}\delta(\lambda - \lambda_{\text{line}}), \quad (\text{A7})$$

where β is the slope of the power-law continuum, F_{line} is the line flux, and λ_{line} is the line wavelength.

Using the filter “x” to “measure” average flux density for this mock spectrum, we get

$$\langle f_\lambda \rangle_x = \frac{\int f_\lambda T_x \lambda \, d\lambda}{\int T_x \lambda \, d\lambda} = \frac{\int f_0(\lambda/\lambda_0)^\beta T_x \lambda \, d\lambda}{\int T_x \lambda \, d\lambda} + \frac{F_{\text{line}} T_x(\lambda_{\text{line}}) \lambda_{\text{line}}}{\int T_x \lambda \, d\lambda} = \frac{f_0}{\lambda_0^\beta} \frac{\langle \lambda^{\beta+1} \rangle_x}{\langle \lambda \rangle_x} + \frac{F_{\text{line}}}{\Delta_x(\lambda_{\text{line}})} \frac{\lambda_{\text{line}}}{\langle \lambda \rangle_x}, \quad (\text{A8})$$

where $\Delta_x(\lambda) \equiv \frac{\int T_x \, d\lambda}{T_x(\lambda)}$ is the effective band width of filter “x” at wavelength λ . Note that this effective band width depends on the wavelength, which equals to the horizontal size of a rectangle with a height equal to the transmission at a given wavelength λ and with the same area that the one covered by the filter transmission curve.

For the two-band scenario, we use a narrowband (NB) and broadband (BB) to capture the line-emitting sources. Therefore, we get linear equations:

$$\begin{cases} \langle f_\lambda \rangle_{\text{NB}} = \frac{f_0}{\lambda_0^\beta} \frac{\langle \lambda^{\beta+1} \rangle_{\text{NB}}}{\langle \lambda \rangle_{\text{NB}}} + \frac{F_{\text{line}}}{\Delta_{\text{NB}}(\lambda_{\text{line}})} \frac{\lambda_{\text{line}}}{\langle \lambda \rangle_{\text{NB}}} \\ \langle f_\lambda \rangle_{\text{BB}} = \frac{f_0}{\lambda_0^\beta} \frac{\langle \lambda^{\beta+1} \rangle_{\text{BB}}}{\langle \lambda \rangle_{\text{BB}}} + \frac{F_{\text{line}}}{\Delta_{\text{BB}}(\lambda_{\text{line}})} \frac{\lambda_{\text{line}}}{\langle \lambda \rangle_{\text{BB}}} \end{cases}. \quad (\text{A9})$$

The solution is

$$\begin{cases} f_{\lambda,\text{cont}}(\lambda) = f_0(\lambda/\lambda_0)^\beta = \frac{\langle f_\lambda \rangle_{\text{NB}} \Delta_{\text{NB}}(\lambda_{\text{line}}) \langle \lambda \rangle_{\text{NB}} \lambda_{\text{line}}^\beta - \langle f_\lambda \rangle_{\text{BB}} \Delta_{\text{BB}}(\lambda_{\text{line}}) \langle \lambda \rangle_{\text{BB}} \lambda_{\text{line}}^\beta}{\Delta_{\text{NB}}(\lambda_{\text{line}}) \langle \lambda^{\beta+1} \rangle_{\text{NB}} - \Delta_{\text{BB}}(\lambda_{\text{line}}) \langle \lambda^{\beta+1} \rangle_{\text{BB}}} (\lambda/\lambda_{\text{line}})^\beta \\ F_{\text{line}} = \left(\langle f_\lambda \rangle_{\text{NB}} \frac{\langle \lambda \rangle_{\text{NB}}}{\langle \lambda^{\beta+1} \rangle_{\text{NB}}} - \langle f_\lambda \rangle_{\text{BB}} \frac{\langle \lambda \rangle_{\text{BB}}}{\langle \lambda^{\beta+1} \rangle_{\text{BB}}} \right) / \left(\frac{\lambda_{\text{line}}}{\Delta_{\text{NB}}(\lambda_{\text{line}}) \langle \lambda^{\beta+1} \rangle_{\text{NB}}} - \frac{\lambda_{\text{line}}}{\Delta_{\text{BB}}(\lambda_{\text{line}}) \langle \lambda^{\beta+1} \rangle_{\text{BB}}} \right). \end{cases} \quad (\text{A10})$$

Because AB magnitude is preferred in galaxy photometry, which is defined as $m_{\text{AB}} = -2.5 \log(f_\nu [\text{erg s}^{-1} \text{cm}^{-2} \text{Hz}^{-1}]) - 48.6$, we present the results in f_ν converting by pivot wavelength:

$$\begin{cases} f_{\lambda,\text{cont}}(\lambda) = f_0(\lambda/\lambda_0)^\beta = \frac{\langle f_\nu \rangle_{\text{NB}} \Delta_{\text{NB}}(\lambda_{\text{line}}) \langle \lambda^{-1} \rangle_{\text{NB}} \lambda_{\text{line}}^\beta - \langle f_\nu \rangle_{\text{BB}} \Delta_{\text{BB}}(\lambda_{\text{line}}) \langle \lambda^{-1} \rangle_{\text{BB}} \lambda_{\text{line}}^\beta}{\Delta_{\text{NB}}(\lambda_{\text{line}}) \langle \lambda^{\beta+1} \rangle_{\text{NB}} - \Delta_{\text{BB}}(\lambda_{\text{line}}) \langle \lambda^{\beta+1} \rangle_{\text{BB}}} c(\lambda/\lambda_{\text{line}})^\beta \\ F_{\text{line}} = c \left(\langle f_\nu \rangle_{\text{NB}} \frac{\langle \lambda^{-1} \rangle_{\text{NB}}}{\langle \lambda^{\beta+1} \rangle_{\text{NB}}} - \langle f_\nu \rangle_{\text{BB}} \frac{\langle \lambda^{-1} \rangle_{\text{BB}}}{\langle \lambda^{\beta+1} \rangle_{\text{BB}}} \right) / \left(\frac{\lambda_{\text{line}}}{\Delta_{\text{NB}}(\lambda_{\text{line}}) \langle \lambda^{\beta+1} \rangle_{\text{NB}}} - \frac{\lambda_{\text{line}}}{\Delta_{\text{BB}}(\lambda_{\text{line}}) \langle \lambda^{\beta+1} \rangle_{\text{BB}}} \right). \end{cases} \quad (\text{A11})$$

To simplify the equations, we define the coefficients as

$$\begin{aligned}
\epsilon_{\text{cont,NB}} &= \frac{\Delta_{\text{NB}}(\lambda_{\text{line}})\langle\lambda^{-1}\rangle_{\text{NB}}\lambda_{\text{line}}^{\beta+2}}{\Delta_{\text{BB}}(\lambda_{\text{line}})\langle\lambda^{\beta+1}\rangle_{\text{BB}} - \Delta_{\text{NB}}(\lambda_{\text{line}})\langle\lambda^{\beta+1}\rangle_{\text{NB}}}, \\
\epsilon_{\text{cont,BB}} &= \frac{\Delta_{\text{BB}}(\lambda_{\text{line}})\langle\lambda^{-1}\rangle_{\text{BB}}\lambda_{\text{line}}^{\beta+2}}{\Delta_{\text{BB}}(\lambda_{\text{line}})\langle\lambda^{\beta+1}\rangle_{\text{BB}} - \Delta_{\text{NB}}(\lambda_{\text{line}})\langle\lambda^{\beta+1}\rangle_{\text{NB}}}, \\
\epsilon_{\text{line,NB}} &= \frac{\lambda_{\text{line}}\langle\lambda^{-1}\rangle_{\text{NB}}}{\langle\lambda^{\beta+1}\rangle_{\text{NB}}} / \left(\frac{1}{\Delta_{\text{NB}}(\lambda_{\text{line}})\langle\lambda^{\beta+1}\rangle_{\text{NB}}} - \frac{1}{\Delta_{\text{BB}}(\lambda_{\text{line}})\langle\lambda^{\beta+1}\rangle_{\text{BB}}} \right), \\
\epsilon_{\text{line,BB}} &= \frac{\lambda_{\text{line}}\langle\lambda^{-1}\rangle_{\text{BB}}}{\langle\lambda^{\beta+1}\rangle_{\text{BB}}} / \left(\frac{1}{\Delta_{\text{NB}}(\lambda_{\text{line}})\langle\lambda^{\beta+1}\rangle_{\text{NB}}} - \frac{1}{\Delta_{\text{BB}}(\lambda_{\text{line}})\langle\lambda^{\beta+1}\rangle_{\text{BB}}} \right).
\end{aligned} \tag{A12}$$

Then the solution will be

$$\begin{cases} f_{\lambda,\text{cont}}(\lambda) = (\epsilon_{\text{cont,BB}}\langle f_{\nu}\rangle_{\text{BB}} - \epsilon_{\text{cont,NB}}\langle f_{\nu}\rangle_{\text{NB}}) \frac{c}{\lambda_{\text{line}}^2} (\lambda/\lambda_{\text{line}})^{\beta} \\ F_{\text{line}} = (\epsilon_{\text{line,NB}}\langle f_{\nu}\rangle_{\text{NB}} - \epsilon_{\text{line,BB}}\langle f_{\nu}\rangle_{\text{BB}}) \frac{c}{\lambda_{\text{line}}^2} \end{cases}. \tag{A13}$$

In this work, we assume a constant continuum f_{ν} , which refers to $\beta = -2$. Therefore, the coefficients can be simplified to be:

$$\begin{aligned}
\epsilon_{\text{cont,NB}} &= \frac{\Delta_{\text{NB}}(\lambda_{\text{line}})\langle\lambda^{-1}\rangle_{\text{NB}}}{\Delta_{\text{BB}}(\lambda_{\text{line}})\langle\lambda^{-1}\rangle_{\text{BB}} - \Delta_{\text{NB}}(\lambda_{\text{line}})\langle\lambda^{-1}\rangle_{\text{NB}}}, \\
\epsilon_{\text{cont,BB}} &= 1 + \epsilon_{\text{cont,NB}} \\
\Delta_{\text{NB;BB}|\lambda_{\text{line}}} \equiv \epsilon_{\text{line,NB}} = \epsilon_{\text{line,BB}} &= \lambda_{\text{line}} \left(\frac{1}{\Delta_{\text{NB}}(\lambda_{\text{line}})\langle\lambda^{-1}\rangle_{\text{NB}}} - \frac{1}{\Delta_{\text{BB}}(\lambda_{\text{line}})\langle\lambda^{-1}\rangle_{\text{BB}}} \right)^{-1},
\end{aligned} \tag{A14}$$

where $\Delta_{\text{NB;BB}|\lambda_{\text{line}}}$ is the calibrated effective bandwidth. The solutions in the assumption can be

$$\begin{cases} f_{\nu,\text{cont}} = \epsilon_{\text{cont,BB}}\langle f_{\nu}\rangle_{\text{BB}} - \epsilon_{\text{cont,NB}}\langle f_{\nu}\rangle_{\text{NB}} \\ F_{\text{line}} = (\langle f_{\nu}\rangle_{\text{NB}} - \langle f_{\nu}\rangle_{\text{BB}}) \frac{c\Delta_{\text{NB;BB}|\lambda_{\text{line}}}}{\lambda_{\text{line}}^2} \end{cases} \tag{A15}$$

We use the pivot wavelength of the NB as the line wavelength. For the NB400 and g-band, the coefficients are:

$$\begin{aligned}
\epsilon_{\text{cont,NB400}} &= 0.027, \\
\epsilon_{\text{cont,g}} &= 1.027, \\
\epsilon_{\text{line,NB400}} = \epsilon_{\text{line,g}} &= 101.0 \text{ \AA}.
\end{aligned} \tag{A16}$$

For the NB387 and g-band, the coefficients are:

$$\begin{aligned}
\epsilon_{\text{cont,NB387}} &= 0, \\
\epsilon_{\text{cont,g}} &= 1, \\
\epsilon_{\text{line,NB387}} = \epsilon_{\text{line,g}} &= 55.9 \text{ \AA}.
\end{aligned} \tag{A17}$$

REFERENCES

- Aihara, H., AlSayyad, Y., Ando, M., et al. 2019, PASJ, 71, 114, doi: [10.1093/pasj/psz103](https://doi.org/10.1093/pasj/psz103)
—, 2022, PASJ, 74, 247, doi: [10.1093/pasj/psab122](https://doi.org/10.1093/pasj/psab122)



























- Ao, Y., Zheng, Z., Henkel, C., et al. 2020, *NatAs*, 4, 670, doi: [10.1038/s41550-020-1033-3](https://doi.org/10.1038/s41550-020-1033-3)
- Arrigoni Battaia, F., Hennawi, J. F., Cantalupo, S., & Prochaska, J. X. 2016, *ApJ*, 829, 3, doi: [10.3847/0004-637X/829/1/3](https://doi.org/10.3847/0004-637X/829/1/3)
- Arrigoni Battaia, F., Hennawi, J. F., Prochaska, J. X., et al. 2019, *MNRAS*, 482, 3162, doi: [10.1093/mnras/sty2827](https://doi.org/10.1093/mnras/sty2827)
- Arrigoni Battaia, F., Prochaska, J. X., Hennawi, J. F., et al. 2018a, *MNRAS*, 473, 3907, doi: [10.1093/mnras/stx2465](https://doi.org/10.1093/mnras/stx2465)
- Arrigoni Battaia, F., Chen, C.-C., Fumagalli, M., et al. 2018b, *A&A*, 620, A202, doi: [10.1051/0004-6361/201834195](https://doi.org/10.1051/0004-6361/201834195)
- Barger, A. J., Cowie, L. L., & Wold, I. G. B. 2012, *ApJ*, 749, 106, doi: [10.1088/0004-637X/749/2/106](https://doi.org/10.1088/0004-637X/749/2/106)
- Bertin, E. 2011, in *Astronomical Society of the Pacific Conference Series*, Vol. 442, *Astronomical Data Analysis Software and Systems XX*, ed. I. N. Evans, A. Accomazzi, D. J. Mink, & A. H. Rots, 435
- Bertin, E., & Arnouts, S. 1996, *A&AS*, 117, 393, doi: [10.1051/aas:1996164](https://doi.org/10.1051/aas:1996164)
- Bessell, M. S. 1990, *PASP*, 102, 1181, doi: [10.1086/132749](https://doi.org/10.1086/132749)
- Boquien, M., Burgarella, D., Roehlly, Y., et al. 2019, *A&A*, 622, A103, doi: [10.1051/0004-6361/201834156](https://doi.org/10.1051/0004-6361/201834156)
- Borisova, E., Cantalupo, S., Lilly, S. J., et al. 2016, *ApJ*, 831, 39, doi: [10.3847/0004-637X/831/1/39](https://doi.org/10.3847/0004-637X/831/1/39)
- Bosch, J., Armstrong, R., Bickerton, S., et al. 2018, *PASJ*, 70, S5, doi: [10.1093/pasj/psx080](https://doi.org/10.1093/pasj/psx080)
- Bridge, C. R., Blain, A., Borys, C. J. K., et al. 2013, *ApJ*, 769, 91, doi: [10.1088/0004-637X/769/2/91](https://doi.org/10.1088/0004-637X/769/2/91)
- Bruzual, G., & Charlot, S. 2003, *MNRAS*, 344, 1000, doi: [10.1046/j.1365-8711.2003.06897.x](https://doi.org/10.1046/j.1365-8711.2003.06897.x)
- Bădescu, T., Yang, Y., Bertoldi, F., et al. 2017, *ApJ*, 845, 172, doi: [10.3847/1538-4357/aa8220](https://doi.org/10.3847/1538-4357/aa8220)
- Cai, Z., Fan, X., Peirani, S., et al. 2016, *ApJ*, 833, 135, doi: [10.3847/1538-4357/833/2/135](https://doi.org/10.3847/1538-4357/833/2/135)
- Cai, Z., Fan, X., Yang, Y., et al. 2017a, *ApJ*, 837, 71, doi: [10.3847/1538-4357/aa5d14](https://doi.org/10.3847/1538-4357/aa5d14)
- Cai, Z., Fan, X., Bian, F., et al. 2017b, *ApJ*, 839, 131, doi: [10.3847/1538-4357/aa6a1a](https://doi.org/10.3847/1538-4357/aa6a1a)
- Cai, Z., Hamden, E., Matuszewski, M., et al. 2018, *ApJL*, 861, L3, doi: [10.3847/2041-8213/aacce6](https://doi.org/10.3847/2041-8213/aacce6)
- Cai, Z., Cantalupo, S., Prochaska, J. X., et al. 2019, *ApJS*, 245, 23, doi: [10.3847/1538-4365/ab4796](https://doi.org/10.3847/1538-4365/ab4796)
- Calzetti, D., Armus, L., Bohlin, R. C., et al. 2000, *ApJ*, 533, 682, doi: [10.1086/308692](https://doi.org/10.1086/308692)
- Caminha, G. B., Karman, W., Rosati, P., et al. 2016, *A&A*, 595, A100, doi: [10.1051/0004-6361/201527995](https://doi.org/10.1051/0004-6361/201527995)
- Cantalupo, S., Arrigoni-Battaia, F., Prochaska, J. X., Hennawi, J. F., & Madau, P. 2014, *Natur*, 506, 63, doi: [10.1038/nature12898](https://doi.org/10.1038/nature12898)
- Cantalupo, S., Lilly, S. J., & Haehnelt, M. G. 2012, *MNRAS*, 425, 1992, doi: [10.1111/j.1365-2966.2012.21529.x](https://doi.org/10.1111/j.1365-2966.2012.21529.x)
- Cantalupo, S., Porciani, C., Lilly, S. J., & Miniati, F. 2005, *ApJ*, 628, 61, doi: [10.1086/430758](https://doi.org/10.1086/430758)
- Cen, R., & Zheng, Z. 2013, *ApJ*, 775, 112, doi: [10.1088/0004-637X/775/2/112](https://doi.org/10.1088/0004-637X/775/2/112)
- Colbert, J. W., Scarlata, C., Teplitz, H., et al. 2011, *ApJ*, 728, 59, doi: [10.1088/0004-637X/728/1/59](https://doi.org/10.1088/0004-637X/728/1/59)
- Condon, J. J., Cotton, W. D., Greisen, E. W., et al. 1998, *AJ*, 115, 1693, doi: [10.1086/300337](https://doi.org/10.1086/300337)
- Daddi, E., Valentino, F., Rich, R. M., et al. 2021, *A&A*, 649, A78, doi: [10.1051/0004-6361/202038700](https://doi.org/10.1051/0004-6361/202038700)
- Daddi, E., Rich, R. M., Valentino, F., et al. 2022, *ApJL*, 926, L21, doi: [10.3847/2041-8213/ac531f](https://doi.org/10.3847/2041-8213/ac531f)
- Dale, D. A., Helou, G., Magdis, G. E., et al. 2014, *ApJ*, 784, 83, doi: [10.1088/0004-637X/784/1/83](https://doi.org/10.1088/0004-637X/784/1/83)
- Dannerbauer, H., Kurk, J. D., De Breuck, C., et al. 2014, *A&A*, 570, A55, doi: [10.1051/0004-6361/201423771](https://doi.org/10.1051/0004-6361/201423771)
- de Gasperin, F., Intema, H. T., & Frail, D. A. 2018, *MNRAS*, 474, 5008, doi: [10.1093/mnras/stx3125](https://doi.org/10.1093/mnras/stx3125)
- Dey, A., Bian, C., Soifer, B. T., et al. 2005, *ApJ*, 629, 654, doi: [10.1086/430775](https://doi.org/10.1086/430775)
- Dey, A., Soifer, B. T., Desai, V., et al. 2008, *ApJ*, 677, 943, doi: [10.1086/529516](https://doi.org/10.1086/529516)
- Dijkstra, M., & Loeb, A. 2009, *MNRAS*, 400, 1109, doi: [10.1111/j.1365-2966.2009.15533.x](https://doi.org/10.1111/j.1365-2966.2009.15533.x)
- Dressler, A., Bigelow, B., Hare, T., et al. 2011, *PASP*, 123, 288, doi: [10.1086/658908](https://doi.org/10.1086/658908)
- Eisenhardt, P. R. M., Wu, J., Tsai, C.-W., et al. 2012, *ApJ*, 755, 173, doi: [10.1088/0004-637X/755/2/173](https://doi.org/10.1088/0004-637X/755/2/173)
- Erb, D. K., Bogosavljević, M., & Steidel, C. C. 2011, *ApJL*, 740, L31, doi: [10.1088/2041-8205/740/1/L31](https://doi.org/10.1088/2041-8205/740/1/L31)
- Evans, I. N., Primini, F. A., Glotfelty, K. J., et al. 2010, *ApJS*, 189, 37, doi: [10.1088/0067-0049/189/1/37](https://doi.org/10.1088/0067-0049/189/1/37)
- Fabricant, D., Fata, R., Epps, H., et al. 2019, *PASP*, 131, 075004, doi: [10.1088/1538-3873/ab1d78](https://doi.org/10.1088/1538-3873/ab1d78)
- Fardal, M. A., Katz, N., Gardner, J. P., et al. 2001, *ApJ*, 562, 605, doi: [10.1086/323519](https://doi.org/10.1086/323519)
- Farina, E. P., Arrigoni-Battaia, F., Costa, T., et al. 2019, *ApJ*, 887, 196, doi: [10.3847/1538-4357/ab5847](https://doi.org/10.3847/1538-4357/ab5847)
- Faucher-Giguère, C.-A., Kereš, D., Dijkstra, M., Hernquist, L., & Zaldarriaga, M. 2010, *ApJ*, 725, 633, doi: [10.1088/0004-637X/725/1/633](https://doi.org/10.1088/0004-637X/725/1/633)
- Faucher-Giguère, C.-A., & Oh, S. P. 2023, *ARA&A*, 61, 131, doi: [10.1146/annurev-astro-052920-125203](https://doi.org/10.1146/annurev-astro-052920-125203)
- Flesch, E. W. 2021, *arXiv*, arXiv:2105.12985, doi: [10.48550/arXiv.2105.12985](https://doi.org/10.48550/arXiv.2105.12985)
- Flewelling, H. A., Magnier, E. A., Chambers, K. C., et al. 2020, *ApJS*, 251, 7, doi: [10.3847/1538-4365/abb82d](https://doi.org/10.3847/1538-4365/abb82d)

- Francis, P. J., Williger, G. M., Collins, N. R., et al. 2001, *ApJ*, 554, 1001, doi: [10.1086/321417](https://doi.org/10.1086/321417)
- Fukugita, M., Ichikawa, T., Gunn, J. E., et al. 1996, *AJ*, 111, 1748, doi: [10.1086/117915](https://doi.org/10.1086/117915)
- Fynbo, J. U., Møller, P., & Warren, S. J. 1999, *MNRAS*, 305, 849, doi: [10.1046/j.1365-8711.1999.02520.x](https://doi.org/10.1046/j.1365-8711.1999.02520.x)
- Geach, J. E., Alexander, D. M., Lehmer, B. D., et al. 2009, *ApJ*, 700, 1, doi: [10.1088/0004-637X/700/1/1](https://doi.org/10.1088/0004-637X/700/1/1)
- Ginolfi, M., Piconcelli, E., Zappacosta, L., et al. 2022, *NatCo*, 13, 4574, doi: [10.1038/s41467-022-32297-x](https://doi.org/10.1038/s41467-022-32297-x)
- Haiman, Z., Spaans, M., & Quataert, E. 2000, *ApJL*, 537, L5, doi: [10.1086/312754](https://doi.org/10.1086/312754)
- Hatch, N. A., Overzier, R. A., Kurk, J. D., et al. 2009, *MNRAS*, 395, 114, doi: [10.1111/j.1365-2966.2009.14525.x](https://doi.org/10.1111/j.1365-2966.2009.14525.x)
- Hayes, M., Scarlata, C., & Siana, B. 2011, *Natur*, 476, 304, doi: [10.1038/nature10320](https://doi.org/10.1038/nature10320)
- Heckman, T. M., Lehnert, M. D., Miley, G. K., & van Breugel, W. 1991, *ApJ*, 381, 373, doi: [10.1086/170660](https://doi.org/10.1086/170660)
- Helfand, D. J., White, R. L., & Becker, R. H. 2015, *ApJ*, 801, 26, doi: [10.1088/0004-637X/801/1/26](https://doi.org/10.1088/0004-637X/801/1/26)
- Hennawi, J. F., Prochaska, J. X., Cantalupo, S., & Arrigoni-Battaia, F. 2015, *Sci*, 348, 779, doi: [10.1126/science.aaa5397](https://doi.org/10.1126/science.aaa5397)
- Hibon, P., Tang, F., & Thomas, R. 2020, *A&A*, 641, A32, doi: [10.1051/0004-6361/201936542](https://doi.org/10.1051/0004-6361/201936542)
- Hogg, D. W., Cohen, J. G., Blandford, R., & Pahre, M. A. 1998, *ApJ*, 504, 622, doi: [10.1086/306122](https://doi.org/10.1086/306122)
- Hopkins, P. F., Hernquist, L., Cox, T. J., & Kereš, D. 2008, *ApJS*, 175, 356, doi: [10.1086/524362](https://doi.org/10.1086/524362)
- Hu, E. M., & Cowie, L. L. 1987, *ApJL*, 317, L7, doi: [10.1086/184902](https://doi.org/10.1086/184902)
- Intema, H. T., Jagannathan, P., Mooley, K. P., & Frail, D. A. 2017, *A&A*, 598, A78, doi: [10.1051/0004-6361/201628536](https://doi.org/10.1051/0004-6361/201628536)
- Ishikawa, Y., Wang, B., Zakamska, N. L., et al. 2023, *MNRAS*, 522, 350, doi: [10.1093/mnras/stad1035](https://doi.org/10.1093/mnras/stad1035)
- Jiménez-Andrade, E. F., Cantalupo, S., Magnelli, B., et al. 2023, *MNRAS*, 521, 2326, doi: [10.1093/mnras/stad594](https://doi.org/10.1093/mnras/stad594)
- Kansky, J., Chilingarian, I., Fabricant, D., et al. 2019, *PASP*, 131, 075005, doi: [10.1088/1538-3873/ab1ceb](https://doi.org/10.1088/1538-3873/ab1ceb)
- Keel, W. C., Cohen, S. H., Windhorst, R. A., & Waddington, I. 1999, *AJ*, 118, 2547, doi: [10.1086/301139](https://doi.org/10.1086/301139)
- Kerutt, J., Wisotzki, L., Verhamme, A., et al. 2022, *A&A*, 659, A183, doi: [10.1051/0004-6361/202141900](https://doi.org/10.1051/0004-6361/202141900)
- Kikuta, S., Imanishi, M., Matsuoka, Y., et al. 2017, *ApJ*, 841, 128, doi: [10.3847/1538-4357/aa72f0](https://doi.org/10.3847/1538-4357/aa72f0)
- Kikuta, S., Matsuda, Y., Cen, R., et al. 2019, *PASJ*, 71, L2, doi: [10.1093/pasj/psz055](https://doi.org/10.1093/pasj/psz055)
- Kikuta, S., Matsuda, Y., Inoue, S., et al. 2023, *ApJ*, 947, 75, doi: [10.3847/1538-4357/acbf30](https://doi.org/10.3847/1538-4357/acbf30)
- Kimock, B., Narayanan, D., Smith, A., et al. 2021, *ApJ*, 909, 119, doi: [10.3847/1538-4357/abbe89](https://doi.org/10.3847/1538-4357/abbe89)
- Kollmeier, J. A., Zheng, Z., Davé, R., et al. 2010, *ApJ*, 708, 1048, doi: [10.1088/0004-637X/708/2/1048](https://doi.org/10.1088/0004-637X/708/2/1048)
- Koornneef, J., Bohlin, R., Buser, R., Horne, K., & Turnshek, D. 1986, *HiA*, 7, 833
- Kurk, J. D., Röttgering, H. J. A., Pentericci, L., et al. 2000, *A&A*, 358, L1, doi: [10.48550/arXiv.astro-ph/0005058](https://doi.org/10.48550/arXiv.astro-ph/0005058)
- Kusakabe, H., Verhamme, A., Blaizot, J., et al. 2022, *A&A*, 660, A44, doi: [10.1051/0004-6361/202142302](https://doi.org/10.1051/0004-6361/202142302)
- Lacy, M., Baum, S. A., Chandler, C. J., et al. 2020, *PASP*, 132, 035001, doi: [10.1088/1538-3873/ab63eb](https://doi.org/10.1088/1538-3873/ab63eb)
- Leclercq, F., Bacon, R., Wisotzki, L., et al. 2017, *A&A*, 608, A8, doi: [10.1051/0004-6361/201731480](https://doi.org/10.1051/0004-6361/201731480)
- Li, J., Emonts, B. H. C., Cai, Z., et al. 2021, *ApJL*, 922, L29, doi: [10.3847/2041-8213/ac390d](https://doi.org/10.3847/2041-8213/ac390d)
- Li, M. 2023, MyFilter: A Web Application for Interactive Visualization of Astronomical Filter Transmission Curves, 1.0.0, Zenodo, doi: [10.5281/zenodo.10210201](https://doi.org/10.5281/zenodo.10210201)
- Liang, Y., Kashikawa, N., Cai, Z., et al. 2021, *ApJ*, 907, 3, doi: [10.3847/1538-4357/abcd93](https://doi.org/10.3847/1538-4357/abcd93)
- Liang, Y., Ouchi, M., Sun, D., et al. 2024, *arXiv*, arXiv:2404.15963, doi: [10.48550/arXiv.2404.15963](https://doi.org/10.48550/arXiv.2404.15963)
- Liu, W., Veilleux, S., Rupke, D. S. N., et al. 2022, *ApJ*, 934, 160, doi: [10.3847/1538-4357/ac7a46](https://doi.org/10.3847/1538-4357/ac7a46)
- Lyke, B. W., Higley, A. N., McLane, J. N., et al. 2020, *ApJS*, 250, 8, doi: [10.3847/1538-4365/aba623](https://doi.org/10.3847/1538-4365/aba623)
- Lyu, J., Alberts, S., Rieke, G. H., & Rujopakarn, W. 2022, *ApJ*, 941, 191, doi: [10.3847/1538-4357/ac9e5d](https://doi.org/10.3847/1538-4357/ac9e5d)
- Ma, K., Zhang, H., Cai, Z., et al. 2024, *ApJ*, 961, 102, doi: [10.3847/1538-4357/ad04da](https://doi.org/10.3847/1538-4357/ad04da)
- Mackenzie, R., Pezzulli, G., Cantalupo, S., et al. 2021, *MNRAS*, 502, 494, doi: [10.1093/mnras/staa3277](https://doi.org/10.1093/mnras/staa3277)
- Martin, D. C., Darvish, B., Lin, Z., et al. 2023, *NatAs*, 7, 1390, doi: [10.1038/s41550-023-02054-1](https://doi.org/10.1038/s41550-023-02054-1)
- Matsuda, Y., Yamada, T., Hayashino, T., et al. 2004, *AJ*, 128, 569, doi: [10.1086/422020](https://doi.org/10.1086/422020)
- . 2005, *ApJL*, 634, L125, doi: [10.1086/499071](https://doi.org/10.1086/499071)
- Matsuda, Y., Nakamura, Y., Morimoto, N., et al. 2009, *MNRAS*, 400, L66, doi: [10.1111/j.1745-3933.2009.00764.x](https://doi.org/10.1111/j.1745-3933.2009.00764.x)
- Matsuda, Y., Yamada, T., Hayashino, T., et al. 2011, *MNRAS*, 410, L13, doi: [10.1111/j.1745-3933.2010.00969.x](https://doi.org/10.1111/j.1745-3933.2010.00969.x)
- Mayo, J. H., Vernet, J., De Breuck, C., et al. 2012, *A&A*, 539, A33, doi: [10.1051/0004-6361/201118254](https://doi.org/10.1051/0004-6361/201118254)
- McCarthy, P. J. 1993, *ARA&A*, 31, 639, doi: [10.1146/annurev.aa.31.090193.003231](https://doi.org/10.1146/annurev.aa.31.090193.003231)
- McCarthy, P. J., Spinrad, H., Djorgovski, S., et al. 1987, *ApJL*, 319, L39, doi: [10.1086/184951](https://doi.org/10.1086/184951)
- Miley, G. K., Overzier, R. A., Zirm, A. W., et al. 2006, *ApJL*, 650, L29, doi: [10.1086/508534](https://doi.org/10.1086/508534)

- Miyazaki, S., Komiyama, Y., Kawanomoto, S., et al. 2018, PASJ, 70, S1, doi: [10.1093/pasj/psx063](https://doi.org/10.1093/pasj/psx063)
- Napolitano, L., Pandey, A., Myers, A. D., et al. 2023, AJ, 166, 99, doi: [10.3847/1538-3881/ace62c](https://doi.org/10.3847/1538-3881/ace62c)
- Nilsson, K. K., Fynbo, J. P. U., Møller, P., Sommer-Larsen, J., & Ledoux, C. 2006, A&A, 452, L23, doi: [10.1051/0004-6361:200600025](https://doi.org/10.1051/0004-6361:200600025)
- Ning, Y., Jiang, L., Zheng, Z.-Y., & Wu, J. 2022, ApJ, 926, 230, doi: [10.3847/1538-4357/ac4268](https://doi.org/10.3847/1538-4357/ac4268)
- Ning, Y., Jiang, L., Zheng, Z.-Y., et al. 2020, ApJ, 903, 4, doi: [10.3847/1538-4357/abb705](https://doi.org/10.3847/1538-4357/abb705)
- Oemler, A., Clardy, K., Kelson, D., Walth, G., & Villanueva, E. 2017, COSMOS: Carnegie Observatories System for MultiObject Spectroscopy, Astrophysics Source Code Library, record ascl:1705.001
- Oke, J. B. 1974, ApJS, 27, 21, doi: [10.1086/190287](https://doi.org/10.1086/190287)
- Oke, J. B., & Gunn, J. E. 1983, ApJ, 266, 713, doi: [10.1086/160817](https://doi.org/10.1086/160817)
- Ouchi, M., Ono, Y., & Shibuya, T. 2020, ARA&A, 58, 617, doi: [10.1146/annurev-astro-032620-021859](https://doi.org/10.1146/annurev-astro-032620-021859)
- Ouchi, M., Shimasaku, K., Akiyama, M., et al. 2008, ApJS, 176, 301, doi: [10.1086/527673](https://doi.org/10.1086/527673)
- Overzier, R. A., Nesvadba, N. P. H., Dijkstra, M., et al. 2013, ApJ, 771, 89, doi: [10.1088/0004-637X/771/2/89](https://doi.org/10.1088/0004-637X/771/2/89)
- Palunas, P., Teplitz, H. I., Francis, P. J., Williger, G. M., & Woodgate, B. E. 2004, ApJ, 602, 545, doi: [10.1086/381145](https://doi.org/10.1086/381145)
- Pentericci, L., Kurk, J. D., Röttgering, H. J. A., et al. 2000, A&A, 361, L25, doi: [10.48550/arXiv.astro-ph/0008143](https://doi.org/10.48550/arXiv.astro-ph/0008143)
- Prescott, M. K. M., Dey, A., & Jannuzi, B. T. 2009, ApJ, 702, 554, doi: [10.1088/0004-637X/702/1/554](https://doi.org/10.1088/0004-637X/702/1/554)
- . 2012, ApJ, 748, 125, doi: [10.1088/0004-637X/748/2/125](https://doi.org/10.1088/0004-637X/748/2/125)
- Rahna, P. T., Zheng, Z. Y., Chies-Santos, A. L., et al. 2022, A&A, 668, A148, doi: [10.1051/0004-6361/202244711](https://doi.org/10.1051/0004-6361/202244711)
- Ramakrishnan, V., Moon, B., Im, S. H., et al. 2023, ApJ, 951, 119, doi: [10.3847/1538-4357/acd341](https://doi.org/10.3847/1538-4357/acd341)
- Reuland, M., van Breugel, W., Röttgering, H., et al. 2003, ApJ, 592, 755, doi: [10.1086/375619](https://doi.org/10.1086/375619)
- Rosdahl, J., & Blaizot, J. 2012, MNRAS, 423, 344, doi: [10.1111/j.1365-2966.2012.20883.x](https://doi.org/10.1111/j.1365-2966.2012.20883.x)
- Saito, T., Shimasaku, K., Okamura, S., et al. 2006, ApJ, 648, 54, doi: [10.1086/505678](https://doi.org/10.1086/505678)
- Schirmer, M., Malhotra, S., Levenson, N. A., et al. 2016, MNRAS, 463, 1554, doi: [10.1093/mnras/stw1819](https://doi.org/10.1093/mnras/stw1819)
- Shen, X., Hopkins, P. F., Faucher-Giguère, C.-A., et al. 2020, MNRAS, 495, 3252, doi: [10.1093/mnras/staa1381](https://doi.org/10.1093/mnras/staa1381)
- Shi, D. D., Cai, Z., Fan, X., et al. 2021, ApJ, 915, 32, doi: [10.3847/1538-4357/abfec0](https://doi.org/10.3847/1538-4357/abfec0)
- Shibuya, T., Ouchi, M., Harikane, Y., et al. 2018, PASJ, 70, S15, doi: [10.1093/pasj/psx107](https://doi.org/10.1093/pasj/psx107)
- Shimakawa, R. 2022, MNRAS, 514, 3910, doi: [10.1093/mnras/stac1575](https://doi.org/10.1093/mnras/stac1575)
- Shimwell, T. W., Hardcastle, M. J., Tasse, C., et al. 2022, A&A, 659, A1, doi: [10.1051/0004-6361/202142484](https://doi.org/10.1051/0004-6361/202142484)
- Shukla, G., Srianand, R., Gupta, N., et al. 2021, MNRAS, 501, 5362, doi: [10.1093/mnras/staa3977](https://doi.org/10.1093/mnras/staa3977)
- Smith, D. J. B., & Jarvis, M. J. 2007, MNRAS, 378, L49, doi: [10.1111/j.1745-3933.2007.00318.x](https://doi.org/10.1111/j.1745-3933.2007.00318.x)
- Stalevski, M., Fritz, J., Baes, M., Nakos, T., & Popović, L. Č. 2012, MNRAS, 420, 2756, doi: [10.1111/j.1365-2966.2011.19775.x](https://doi.org/10.1111/j.1365-2966.2011.19775.x)
- Stalevski, M., Ricci, C., Ueda, Y., et al. 2016, MNRAS, 458, 2288, doi: [10.1093/mnras/stw444](https://doi.org/10.1093/mnras/stw444)
- Steidel, C. C., Adelberger, K. L., Shapley, A. E., et al. 2000, ApJ, 532, 170, doi: [10.1086/308568](https://doi.org/10.1086/308568)
- Swinbank, A. M., Vernet, J. D. R., Smail, I., et al. 2015, MNRAS, 449, 1298, doi: [10.1093/mnras/stv366](https://doi.org/10.1093/mnras/stv366)
- Tadhunter, C. 2016, A&ARv, 24, 10, doi: [10.1007/s00159-016-0094-x](https://doi.org/10.1007/s00159-016-0094-x)
- Taniguchi, Y., & Shioya, Y. 2000, ApJL, 532, L13, doi: [10.1086/312557](https://doi.org/10.1086/312557)
- Tokunaga, A. T., & Vacca, W. D. 2005, PASP, 117, 1459, doi: [10.1086/499029](https://doi.org/10.1086/499029)
- Tumlinson, J., Peebles, M. S., & Werk, J. K. 2017, ARA&A, 55, 389, doi: [10.1146/annurev-astro-091916-055240](https://doi.org/10.1146/annurev-astro-091916-055240)
- Umehata, H., Fumagalli, M., Smail, I., et al. 2019, Sci, 366, 97, doi: [10.1126/science.aaw5949](https://doi.org/10.1126/science.aaw5949)
- Umehata, H., Smail, I., Steidel, C. C., et al. 2021, ApJ, 918, 69, doi: [10.3847/1538-4357/ac1106](https://doi.org/10.3847/1538-4357/ac1106)
- van Ojik, R., Roettgering, H. J. A., Miley, G. K., & Hunstead, R. W. 1997, A&A, 317, 358, doi: [10.48550/arXiv.astro-ph/9608092](https://doi.org/10.48550/arXiv.astro-ph/9608092)
- Vanzella, E., De Barros, S., Cupani, G., et al. 2016, ApJL, 821, L27, doi: [10.3847/2041-8205/821/2/L27](https://doi.org/10.3847/2041-8205/821/2/L27)
- Venemans, B. P., Röttgering, H. J. A., Miley, G. K., et al. 2007, A&A, 461, 823, doi: [10.1051/0004-6361:20053941](https://doi.org/10.1051/0004-6361:20053941)
- Villar-Martín, M., Sánchez, S. F., Humphrey, A., et al. 2007, MNRAS, 378, 416, doi: [10.1111/j.1365-2966.2007.11811.x](https://doi.org/10.1111/j.1365-2966.2007.11811.x)
- Villar-Martín, M., Tadhunter, C., & Clark, N. 1997, A&A, 323, 21, doi: [10.48550/arXiv.astro-ph/9701016](https://doi.org/10.48550/arXiv.astro-ph/9701016)
- Villar-Martín, M., Vernet, J., di Serego Alighieri, S., et al. 2003, MNRAS, 346, 273, doi: [10.1046/j.1365-2966.2003.07090.x](https://doi.org/10.1046/j.1365-2966.2003.07090.x)
- Wang, W., Wylezalek, D., De Breuck, C., et al. 2021, A&A, 654, A88, doi: [10.1051/0004-6361/202141558](https://doi.org/10.1051/0004-6361/202141558)
- Wang, W., Wylezalek, D., Vernet, J., et al. 2023, A&A, 680, A70, doi: [10.1051/0004-6361/202346415](https://doi.org/10.1051/0004-6361/202346415)

- Webb, N. A., Coriat, M., Traulsen, I., et al. 2020, *A&A*, 641, A136, doi: [10.1051/0004-6361/201937353](https://doi.org/10.1051/0004-6361/201937353)
- White, R. L., Becker, R. H., Helfand, D. J., & Gregg, M. D. 1997, *ApJ*, 475, 479, doi: [10.1086/303564](https://doi.org/10.1086/303564)
- Wright, E. L., Eisenhardt, P. R. M., Mainzer, A. K., et al. 2010, *AJ*, 140, 1868, doi: [10.1088/0004-6256/140/6/1868](https://doi.org/10.1088/0004-6256/140/6/1868)
- Wu, J., Tsai, C.-W., Sayers, J., et al. 2012, *ApJ*, 756, 96, doi: [10.1088/0004-637X/756/1/96](https://doi.org/10.1088/0004-637X/756/1/96)
- Wu, Y., Wang, F., Cai, Z., et al. 2023, *ApJL*, 956, L40, doi: [10.3847/2041-8213/acfee3](https://doi.org/10.3847/2041-8213/acfee3)
- Wylezalek, D., Galametz, A., Stern, D., et al. 2013, *ApJ*, 769, 79, doi: [10.1088/0004-637X/769/1/79](https://doi.org/10.1088/0004-637X/769/1/79)
- Yang, G., Boquien, M., Brandt, W. N., et al. 2022, *ApJ*, 927, 192, doi: [10.3847/1538-4357/ac4971](https://doi.org/10.3847/1538-4357/ac4971)
- Yang, Y., Zabludoff, A., Eisenstein, D., & Davé, R. 2010, *ApJ*, 719, 1654, doi: [10.1088/0004-637X/719/2/1654](https://doi.org/10.1088/0004-637X/719/2/1654)
- Yang, Y., Zabludoff, A., Tremonti, C., Eisenstein, D., & Davé, R. 2009, *ApJ*, 693, 1579, doi: [10.1088/0004-637X/693/2/1579](https://doi.org/10.1088/0004-637X/693/2/1579)
- Zhang, H., Ouchi, M., Itoh, R., et al. 2020, *ApJ*, 891, 177, doi: [10.3847/1538-4357/ab7917](https://doi.org/10.3847/1538-4357/ab7917)
- Zhang, H., Cai, Z., Li, M., et al. 2023a, arXiv, arXiv:2301.07359, doi: [10.48550/arXiv.2301.07359](https://doi.org/10.48550/arXiv.2301.07359)
- Zhang, H., Cai, Z., Liang, Y., et al. 2024, *ApJ*, 961, 63, doi: [10.3847/1538-4357/ad07d3](https://doi.org/10.3847/1538-4357/ad07d3)
- Zhang, S., Cai, Z., Xu, D., et al. 2023b, *ApJ*, 952, 124, doi: [10.3847/1538-4357/acd760](https://doi.org/10.3847/1538-4357/acd760)
- . 2023c, *Sci*, 380, 494, doi: [10.1126/science.abj9192](https://doi.org/10.1126/science.abj9192)
- Zheng, Y., Peebles, M. S., O’Shea, B. W., et al. 2020, *ApJ*, 896, 143, doi: [10.3847/1538-4357/ab960a](https://doi.org/10.3847/1538-4357/ab960a)
- Zhu, G., & Ménard, B. 2013, *ApJ*, 770, 130, doi: [10.1088/0004-637X/770/2/130](https://doi.org/10.1088/0004-637X/770/2/130)
- Zou, S., Jiang, L., Cai, Z., et al. 2024, *ApJ*, 960, 34, doi: [10.3847/1538-4357/ad09b2](https://doi.org/10.3847/1538-4357/ad09b2)

All Authors and Affiliations

MINGYU LI ¹ HAIBIN ZHANG ^{1,2} ZHENG CAI ¹ YONGMING LIANG ³ NOBUNARI KASHIKAWA ^{2,4,5} KE MA ¹
XIAOHUI FAN ⁶ J. XAVIER PROCHASKA ^{7,8} BJORN H. C. EMONTS ⁹ XIN WANG ^{10,11,12} YUNJING WU ^{1,6}
SHIWU ZHANG ^{1,13} QIONG LI ¹⁴ SEAN D. JOHNSON ¹⁵ MINGHAO YUE ^{16,6} FABRIZIO ARRIGONI BATTALA ¹⁷
SEBASTIANO CANTALUPO ¹⁸ JOSEPH F. HENNAWI ^{19,20} SATOSHI KIKUTA ⁴ YUANHANG NING ¹
MASAMI OUCHI ^{3,2,21} RHYTHM SHIMAKAWA ²² BEN WANG ^{1,19} WEICHEN WANG ¹⁸ ZHENG ZHENG ²³ AND
ZHEN-YA ZHENG ²⁴

¹Department of Astronomy, Tsinghua University, Beijing 100084, People's Republic of China

²National Astronomical Observatory of Japan, 2-21-1 Osawa, Mitaka, Tokyo 181-8588, Japan

³Institute for Cosmic Ray Research, The University of Tokyo, Kashiwa, Chiba 277-8582, Japan

⁴Department of Astronomy, School of Science, The University of Tokyo, 7-3-1 Hongo, Bunkyo-ku, Tokyo 113-0033, Japan

⁵Research Center for the Early Universe, The University of Tokyo, 7-3-1 Hongo, Bunkyo-ku, Tokyo 113-0033, Japan

⁶Steward Observatory, University of Arizona, 933 North Cherry Avenue, Tucson, AZ 85721, USA

⁷Department of Astronomy & Astrophysics, UCO/Lick Observatory, University of California, 1156 High Street, Santa Cruz, CA 95064, USA

⁸Kavli Institute for the Physics and Mathematics of the Universe (Kavli IPMU), 5-1-5 Kashiwanoha, Kashiwa, 277-8583, Japan

⁹National Radio Astronomy Observatory, 520 Edgemont Road, Charlottesville, VA 22903, USA

¹⁰School of Astronomy and Space Science, University of Chinese Academy of Sciences (UCAS), Beijing 100049, China

¹¹National Astronomical Observatories, Chinese Academy of Sciences, Beijing 100101, China

¹²Institute for Frontiers in Astronomy and Astrophysics, Beijing Normal University, Beijing 102206, China

¹³Research Center for Astronomical Computing, Zhejiang Laboratory, Hangzhou 311100, China

¹⁴Jodrell Bank Centre for Astrophysics, University of Manchester, Oxford Road, Manchester, UK

¹⁵Department of Astronomy, University of Michigan, Ann Arbor, MI 48109, USA

¹⁶MIT Kavli Institute for Astrophysics and Space Research, 77 Massachusetts Ave., Cambridge, MA 02139, USA

¹⁷Max-Planck-Institut für Astrophysik, Karl-Schwarzschild-Straße 1, D-85748 Garching bei München, Germany

¹⁸Department of Physics, University of Milan Bicocca, Piazza della Scienza 3, 20126, Milano, Italy

¹⁹Leiden Observatory, Leiden University, P.O. Box 9513, 2300 RA Leiden, The Netherlands

²⁰Department of Physics, Broida Hall, UC Santa Barbara, Santa Barbara, CA 93106-9530, USA

²¹Kavli Institute for the Physics and Mathematics of the Universe (Kavli IPMU, WPI), University of Tokyo, Kashiwa, Chiba 277-8583, Japan

²²Waseda Institute for Advanced Study (WIAS), Waseda University, 1-21-1 Nishi-Waseda, Shinjuku, Tokyo 169-0051, Japan

²³Department of Physics and Astronomy, University of Utah, 115 South 1400 East, Salt Lake City, UT 84112, USA

²⁴Key Laboratory for Research in Galaxies and Cosmology, Shanghai Astronomical Observatory, Chinese Academy of Sciences, 80 Nandan Road, Shanghai 200030, People's Republic of China